Journal of Cosmology and Astroparticle Physics
An IOP and SISSA journal

Received: *February 13, 2024*
Revised: *June 13, 2024*
Accepted: *July 8, 2024*
Published: *July 24, 2024*

A Big Ring on the sky

A.M. Lopez,[a] **R.G. Clowes**[a] **and G.M. Williger**[b]

[a] *Jeremiah Horrocks Institute, University of Central Lancashire, Preston, PR1 2HE, United Kingdom*
[b] *Department of Physics and Astronomy, University of Louisville, Louisville, KY 40292, U.S.A.*

E-mail: amlopez@uclan.ac.uk, rgclowes@uclan.ac.uk, gmwill06@louisville.edu

Abstract: We present the discovery of 'A Big Ring on the Sky' (BR), the second ultra-large large-scale structure (uLSS) found in Mg II-absorber catalogues, following the previously reported Giant Arc (GA). In cosmological terms the BR is close to the GA — at the same redshift $z \sim 0.8$ and with a separation on the sky of only $\sim 12°$. Two extraordinary uLSSs in such close configuration raises the possibility that together they form an even more extraordinary cosmological system. The BR is a striking circular, annulus-like, structure of diameter ~ 400 Mpc (proper size, present epoch). The method of discovery is as described in the GA paper, but here using the new Mg II-absorber catalogues restricted to DR16Q quasars. Using the Convex Hull of Member Spheres (CHMS) algorithm, we estimate that the annulus and inner absorbers of the BR have departures from random expectations, at the density of the control field, of up to 5.2σ. We present the discovery of the BR, assess its significance using the CHMS, Minimal Spanning Tree (MST), FilFinder and Cuzick & Edwards (CE) methods, discuss it in the context of the GA+BR system, and suggest some implications for the origins of uLSS and for our understanding of cosmology. For example, it may be that unusual geometric patterns, such as these uLSSs, have an origin in cosmic strings.

Keywords: cosmic web, superclusters, baryon acoustic oscillations, Cosmic strings, domain walls, monopoles

ArXiv ePrint: 2402.07591

https://doi.org/10.1088/1475-7516/2024/07/055

JCAP07(2024)055

Contents

1 Introduction

We continue to make use of the method of intervening Mg II absorbers in the spectra of quasars to trace faint matter at intermediate redshifts [1, 2]. The Mg II method relies on both the spectroscopic measurement of luminous, high redshift quasars from the Sloan Digital Sky Survey (SDSS), and the highly accurate, spectroscopic redshifts of the intervening Mg II absorption doublets present in the quasar spectra, documented by independent authors [3, 4]. The intervening Mg II absorption doublet indicates the presence of galaxies and galaxy clusters [5–7]. Together, with the quasars and Mg II absorbers, we have the information on the on-sky position of intervening matter and the redshift of the intervening matter, so in mapping the 3D distribution of the Mg II absorption features in the spectra of quasars, we can infer the LSS of intermediate-to-high redshift, faint matter.

The multiple discoveries of LSSs made throughout the past few decades are well known to challenge our understanding of the Standard Cosmological Model (ΛCDM) [2, 8–12], in particular due to a possible violation of a fundamental assumption, the Cosmological Principle (CP), which states that our Universe is both homogeneous and isotropic on large scales. In addition, there are numerous results in cosmology posing similar challenges and tensions for our current standard model (see [13] for a recent review). Large structures in the Universe are interesting for several reasons, such as: how did the structures form so early on in the evolution of the Universe, given the current understanding of CDM structure formation; how

JCAP07(2024)055

might the structures evolve to the present day; do the seeds of such large LSSs lie in the density perturbations that are amplified by inflation [14, 15]. Answers to such questions may lie outside concordance cosmology, with either the inclusion of extensions to the standard model, e.g., cosmic strings (CS) [9, 16–18], or alternative theories to the ΛCDM model, e.g., Conformal Cyclic Cosmology (CCC) [19] and modified gravity theories [20–22].

During the discovery of the Giant Arc (GA) [2] (hereafter Lopez22), the SDSS Data Release 16 quasar database (DR16Q) became available [23]. Then, independent authors created the most up-to-date Mg II database from the DR16Q quasars [3] (hereafter Anand21). Following the discovery of the GA, made using the older Mg II database from [4] (hereafter Z&M, also the corresponding DR7QSO and DR12Q quasar catalogues from [24, 25]), we are now in a position to continue LSS investigations with the new DR16Q database and corresponding DR16Q Mg II database. We have found an interesting ring shape in the Mg II absorbers, indicating a LSS of galaxies and galaxy clusters, that spans a diameter of $\sim 400\,\mathrm{Mpc}$ scaled to the present epoch. Incidentally, the estimated size of the BR is close to that which could be expected in a detection of an individual Baryon Acoustic Oscillation (BAO), $r \sim 150\,\mathrm{Mpc}$ [26–30], but we later suggest that the BR is unlikely to have its origins in BAOs. The BR shape and size are both hard to understand in our current theoretical framework. Additionally, the BR is in the same redshift slice as the GA and to the north of the GA by $\sim 12^\circ$ which raises further questions about their origin both together and independently.

For the work that led to the original discovery of the GA, using the Z&M database, we had looked at only a few small areas of sky and redshift slices [1], essentially to test the viability of the Mg II approach itself. Following the discovery of the GA, and now using the Anand21 database, we have so far concentrated on the GA field and redshift slice because we immediately made the further discovery of the BR there; the only exceptions to this statement are (i) the use of adjacent redshift slices to test that the BR was not arising from artefacts and to test for extensions of the BR into adjacent redshift slices, and (ii) the use of neighbouring fields at the same redshift as the GA/BR field for comparing the spatial clustering results of the Cuzick and Edwards test (see section 3.4). Consequently, a 'look-elsewhere' effect on the statistical assessments should not be a factor. In future, of course, we intend to explore both databases in their entireties.

The Mg II data we use here are complicated and quite difficult to manage. The advantage, of course, is the precise redshifts, and the concomitant possibility of discovering intriguing structures such as the Big Ring and the Giant Arc. In future, the Mg II approach to LSS should be enhanced by DESI spectra [31], taken with the KPNO 4m telescope, allowing detection of Mg II to lower equivalent widths, and hence allowing the exploration of finer detail in the morphology of structures.

In this paper we assess the reality of the BR and its statistical significance with respect to the assumed, homogeneous large-scale distribution of matter.

Note that we have introduced the term 'ultra-large LSS' (uLSS) to distinguish those structures that exceed the estimated $\sim 370\,\mathrm{Mpc}$ upper limit to the scale of homogeneity [32]. This limit is often adopted in discussions of homogeneity and the CP.

JCAP07(2024)055

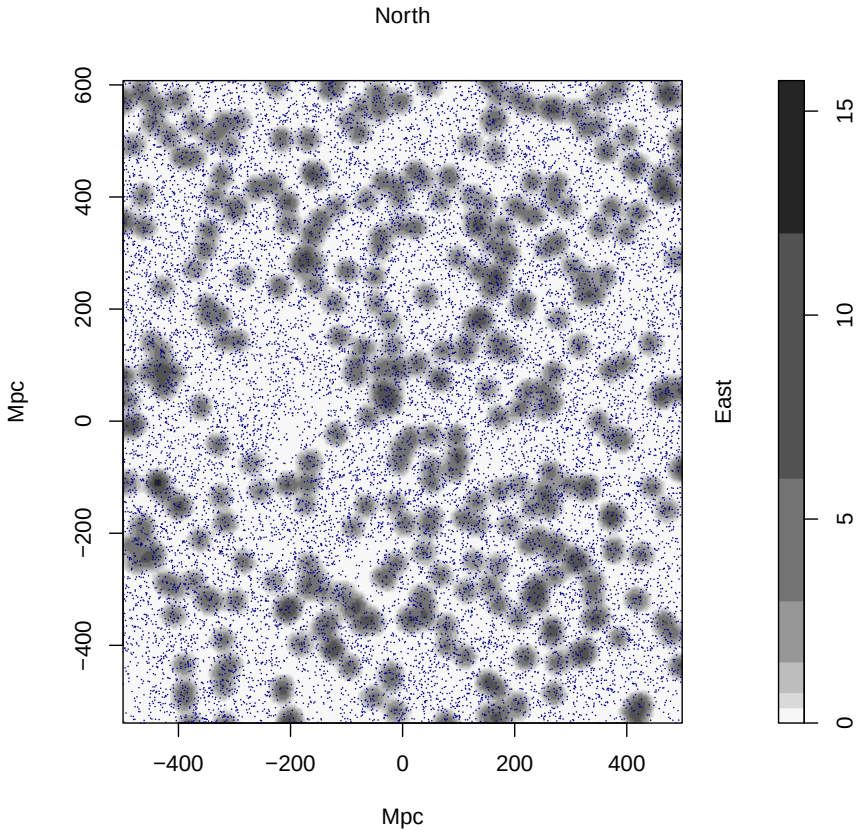

Figure 1. The tangent-plane distribution of Mg II absorbers in the redshift slice $z = 0.802 \pm 0.060$. The grey contours, increasing by a factor of two, represent the density distribution of the absorbers which have been smoothed using a Gaussian kernel of $\sigma = 11\,\mathrm{Mpc}$, and flat-fielded with respect to the distribution of background probes (quasars). The dark blue dots represent the background probes. S/N limits of: $4, 2$ and 4 were applied to the $\lambda_{2796}, \lambda_{2803}$ Mg II lines and quasar continuum, respectively (details of S/N cuts are discussed in section 3.1). The BR can be seen to the north of the centre point spanning $\sim 400\,\mathrm{Mpc}$ in diameter. The field-of-view corresponds to the small, pink area seen in figure 5.

1.1 Cosmological model

The concordance model is adopted for cosmological calculations, with $\Omega_{T0} = 1$, $\Omega_{M0} = 0.27$, $\Omega_{\Lambda 0} = 0.73$, and $H_0 = 70\,\mathrm{km\,s^{-1}\,Mpc^{-1}}$. All sizes given are proper sizes at the present epoch. (For consistency, we are using the same values for the cosmological parameters that were used in Lopez22.)

2 The Big Ring

The existence of a large, circular structure of Mg II absorbers, the Big Ring (BR), became apparent when investigating the new SDSS DR16Q catalogues, and corresponding Mg II databases, at the same redshift and position as the previously documented Giant Arc (GA). In figure 1, we are seeing the BR, which is the visually overdense ring shape of Mg II absorbers centred at approximately $x = 0\,\mathrm{Mpc}$ and $y = 240\,\mathrm{Mpc}$. (The large 'void' to the south-west of the BR is also particularly striking.) In this figure, and others, the grey contours,

JCAP07(2024)055

increasing by a factor of two, represent the density distribution of Mg II absorbers in the specified redshift slice and field-of-view (FOV). The Mg II contours have been smoothed using a Gaussian kernel of $\sigma = 11\,\mathrm{Mpc}$, and flat-fielded with respect to the distribution of background probes (quasars). The smoothing gives a useful impression of the connectivity. The background probes (quasars) are represented by the small, blue points. The axes are labelled in Mpc, scaled to the present epoch; for details on obtaining the Mpc scaling, refer to the GA paper (Lopez22). East is towards the right and north is towards the top. From figure 1 we can estimate the BR diameter is $\sim$ 300–400 Mpc, which would make its circumference comparable to the extent of the GA.

2.1 Data sources

The use of Mg II absorbers for analysing LSS has the particular advantage of providing very precise redshifts. A disadvantage of course, which can require very careful handling, is that one must take the background probes — the quasars — where they are given by the catalogues. The catalogues now have suitably dense coverage on the sky, but generally they are affected by variations in selection criteria.

At $z_{\mathrm{abs}} \sim 0.8$, the parameter in the Anand21 catalogues for the redshift error (Z_ABS_ERR) indicates a median error of $\sigma_{z_{\mathrm{abs}}} \approx 4.2 \times 10^{-5}$. (The emission-redshift error for a quasar catalogue might be about two orders of magnitude larger at ~ 0.004.) This $\sigma_{z_{\mathrm{abs}}}$ corresponds to a velocity difference of $\sim 7\,\mathrm{km\,s^{-1}}$. A comparison of repeated observations in the basic Anand21 database suggests that a practical estimate of the redshift error at $z_{\mathrm{abs}} \sim 0.8$ is a little larger at $\sigma_{z_{\mathrm{abs}}} \approx 1.7 \times 10^{-4}$, corresponding to a velocity difference of $\sim 28\,\mathrm{km\,s^{-1}}$.

When considering the finer details of the morphology of individual LSSs, any blurring will then be due to peculiar velocities, for which plausible values might be $\sim 400\,\mathrm{km\,s^{-1}}$, corresponding to $\sigma_{z_{\mathrm{pec}}} \sim 0.0024$ at $z \sim 0.8$, or $\sim 7\,\mathrm{Mpc}$ in proper distance for the present epoch. We therefore expect that any blurring effects should be minor.

The BR is detected in the new Anand21 Mg II database, whereas the previously documented GA was detected in the older Z&M Mg II database, so we investigate the differences in the databases (e.g. the Mg II absorbers detected from probes that were in common to both databases) in the following manner. First, we choose the standard BR FOV at $z = 0.802 \pm 0.060$ as in figure 1. Then, we select the absorbers and probes arising in the chosen field from both Anand21 and Z&M (making no additional cuts to the S/N or i-magnitude). Using TOPCAT[1] [33], the probe (quasar) and Mg II files are paired in various ways for comparison.

A summary of the results is as follows. (1) There are over three times as many background probes in the field for Anand21 than Z&M. (These are the probes that were initially searched by the authors for Mg II absorbers.) Almost all of the additional probes searched by Anand21 were new observations between SDSS DR12 to DR16. However, a small fraction (just 37 out of 7257 probes) were not included in the Mg II search by Anand21. (2) There are just over twice as many Mg II absorbers detected by Anand21 than by Z&M: 852 Mg II absorbers in Anand21 and 359 Mg II absorbers in Z&M. Of those absorbers, 597 were unique to Anand21 and 104 were unique to Z&M. (3) Of the probes that both authors had in common and

[1] https://www.star.bris.ac.uk/mbt/topcat/.

JCAP07(2024)055

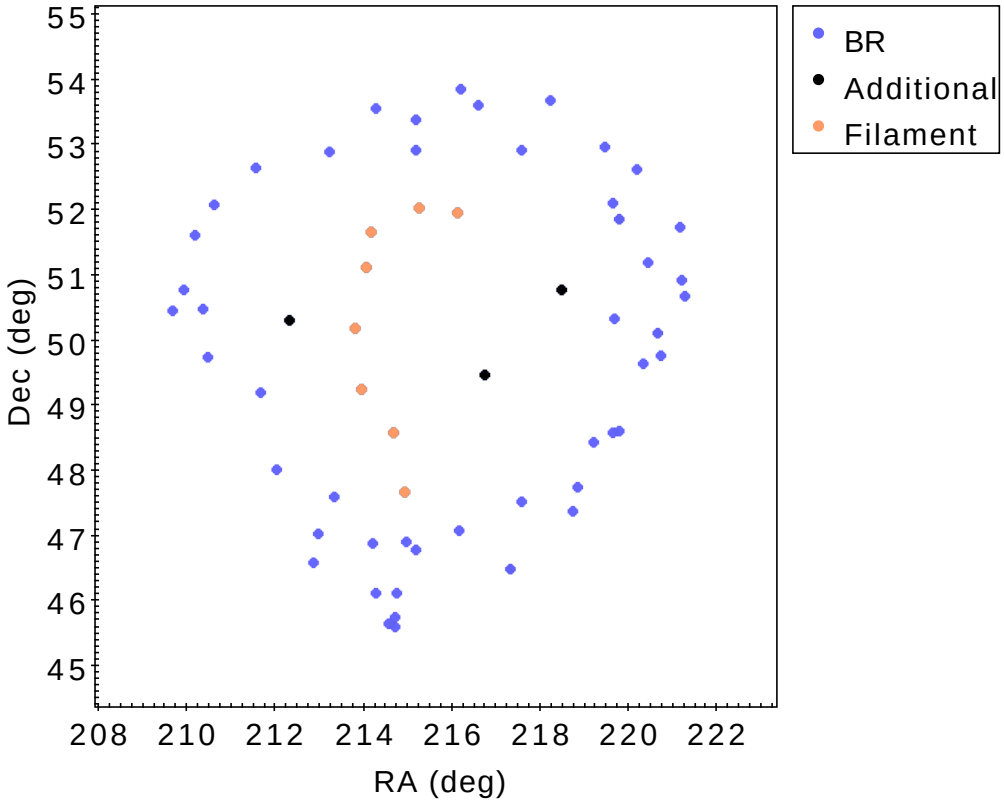

Figure 2. The Mg II absorbers in the visually-identified BR (blue), the inner filament (orange), and the additional absorbers inside the BR (black) from the on-sky perspective. Three of the blue points (BR) correspond to two absorbers occurring in one spectrum (see figure 8).

searched, Anand21 found 67 additional absorbers that Z&M missed, and Z&M found 103 additional absorbers that Anand21 missed. In total, there were 255 Mg II absorbers in common to both authors ($\sim 60\%$ total agreement of the probes in common to both authors). We found that, despite the greater number of absorbers in Anand21, they missed around 1.5 times as many absorbers found by Z&M, compared with the number of absorbers missed by Z&M that were found by Anand21, for shared probes. Without access to their software it will probably remain unclear why Anand21 and Z&M have this disagreement. One possibility might be that Anand21 have more refined search criteria, given that their percentage Mg II detection rate per quasar is much lower than for Z&M. Or, perhaps Z&M are detecting to lower thresholds, without increasing spurious detections.

2.2 Initial checks of the data

First, we check that the Mg II absorbers belonging to the visually-identified BR are real (not false positive detections). We visually inspected spectra of 56 DR16Q quasars that are the probes that correspond to the visually-identified BR and inner filament absorbers (see figure 2). Since 6 of the Mg II absorbers are multiples per probe occurring in three quasar spectra, we were checking for a total of 59 Mg II doublet systems. Each Mg II absorption doublet that we searched for was visually confirmed and in agreement with the documented redshifts from

JCAP07(2024)055

Anand21, so we can confirm that 100% of the Mg II absorber members of the BR and inner filament are real, physical Mg II absorbers indicating the presence of intervening matter.

There are two unusual Mg II systems, occurring in the same spectrum, for which the Anand21-documented redshifts suggest that the λ_{2796} of the lower-z absorption doublet appears at the same wavelength as the λ_{2803} of the higher-z absorption doublet. This is indeed the case: the two Mg II absorption doublets appear as 3 absorption lines in the spectrum, which is a rare oddity. Although Anand21 recognise the 3 absorption lines as two systems, they appear not to have disentangled the EWs of the centre absorption line of the triplet (the higher-z λ_{2796} and the lower-z λ_{2803} EWs being the same).

Secondly, we investigate if the visually obvious BR is an artefact of the probes. This can be done in two ways: simply checking the density distribution of background probes and checking for obvious artefacts; and looking at the next redshift slice down from the BR field (on the near side) and checking for repeating Mg II features that correspond to any obvious artefacts in the probes. For the former, see figure 3.

Many overdensities and underdensities can be seen clearly in figure 3. In particular, there are a few overdense regions (small, dark clumps) centred at 0 Mpc on the x-axis and between roughly 100 Mpc to 400 Mpc on the y-axis, a few of which appear to coincide with the inner filament of BR. This could imply that the inner filament of the BR is suspect, so we will need to be sure that the filament is not an artefact of the probes. We can visually check the rate of occurrence of Mg II absorbers at the position of the overdense artefacts (dense blobs) by blinking the image of the probes (figure 3) with the image of the absorbers (figure 1). Doing this shows that 8 out of 20 randomly selected overdense artefacts had Mg II absorbers present, so less than half of the artefacts. Incidentally, we could also confirm that most of the artefacts that appeared to coincide with parts of the BR (including the inner filament) were in fact offset, so not responsible for the Mg II absorbers arising there. Checking the artefacts shows that there is no particular association of the artefacts with the Mg II absorbers present in the BR field. There is also a much larger region of underdense probes spanning -100 Mpc to 400 Mpc in the y-axis and centred at -200 Mpc in the x-axis which partially coincides with the l.h.s. of the BR. The fact that part of the BR is located in an underdense region of probes is noteworthy.

For the latter way to test if the MgII absorbers are artefacts of the probes, we can check the absorbers arising from the same set of probes corresponding to the BR field in the next, non-overlapping redshift slice on the near side of the BR. To do this we keep the probes of the BR field the same (having $z > 0.862$ — i.e., a redshift greater than the far edge of the BR Mg II redshift slice) and map the Mg II absorption in the nearest, non-overlapping redshift slice (i.e., $z = 0.682 \pm 0.060$). In this way we are able to search for any obvious artefacts of the probes that could be responsible for the specific distribution of Mg II absorbers in the BR field by comparing the Mg II image in the usual BR field with the neighbouring redshift slice. We apply the SLHC/CHMS and FilFinder algorithms to the field centred at $z = 0.682 \pm 0.060$ and corresponding to the usual BR FOV (see sections 3.1 and 3.3 for details on the SLHC/CHMS and FilFinder methods). In the redshift slice $z = 0.682 \pm 0.060$ we find with the SLHC/CHMS method that there are no structures detected by the SLHC algorithm corresponding to the BR, and in addition, no structures at all that are statistically significant.

JCAP07(2024)055

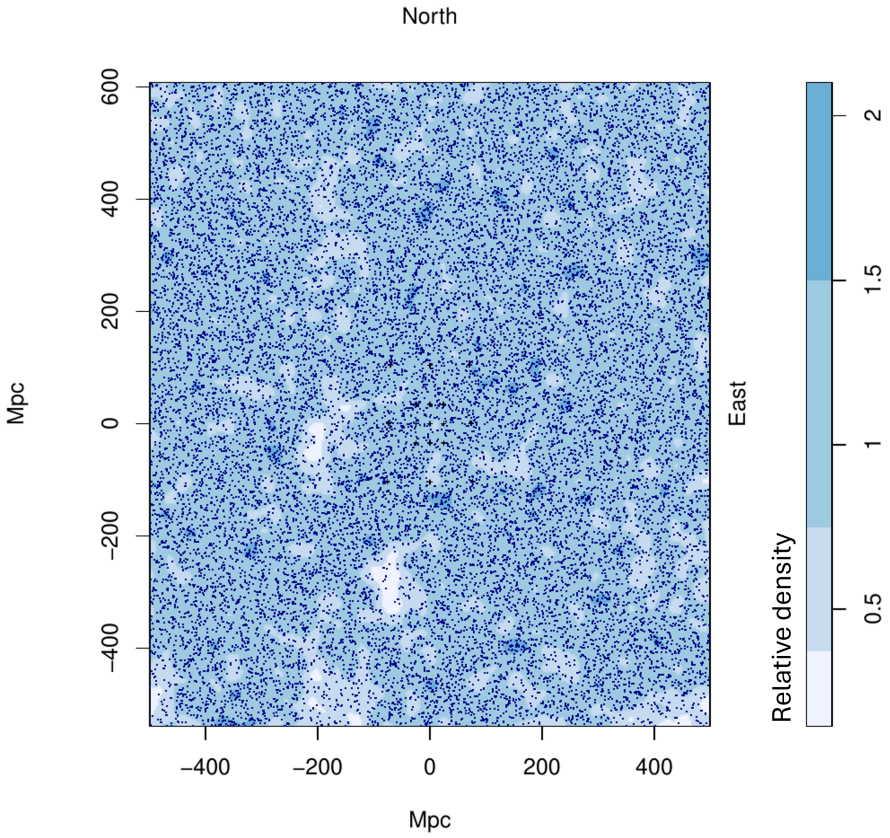

Figure 3. The tangent-plane distribution of probes (background quasars) in the BR FOV with the redshift condition $z > 0.862$ — i.e., the probes that are responsible for the Mg II absorbers arising in the BR field. The blue contours, increasing by a factor of two, represent the density distribution of the probes which have been smoothed using a Gaussian kernel of $\sigma = 11$ Mpc. S/N limits were applied to the quasar continuum such that $S/N_{con} > 4$ (details of S/N are discussed in section 3.1). The field-of-view corresponds to the small, pink area seen in figure 5. The figure shows many areas of overdensities and underdensities. In particular, there are a few overdense regions (small, dark clumps), centred at 0 Mpc on the x-axis and between roughly 100 Mpc to 400 Mpc on the y-axis, a few of which appear to coincide with the inner filament of BR. There is also a much larger region of underdense probes spanning −100 Mpc to 400 Mpc in the y-axis and centred at −200 Mpc in the x-axis which coincides with the l.h.s. of the BR.

We also find with the FilFinder method, no filaments detected in the field that correspond to the BR (figure 4). Therefore, we conclude that the BR is not an artefact of the probes.

It is worth highlighting that the BR appears in the same redshift slice and FOV as the previously documented GA, but we are now using the new Anand21 databases and not the previously used Z&M databases. As mentioned earlier, the overall agreement between the two datasets is $\sim 60\%$ for the probes in common in the BR field, so the GA appears somewhat different in this new dataset. The GA is still the most significant, most numerous and overdense structure detected in the field despite the slight change in appearance, so quantitatively, there is very little difference in the GA in the new dataset. However, qualitatively, there are two main reasons the GA appears different: (1) the field overall is much more dense with the new dataset due to many more quasar observations; (2) Anand21 miss several GA absorbers. We

JCAP07(2024)055

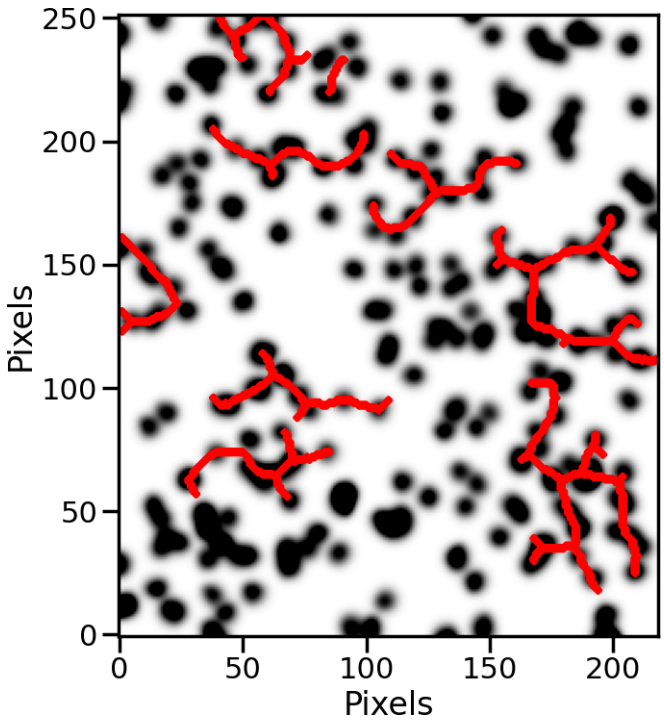

Figure 4. The FilFinder algorithm applied to the tangent-plane distribution of Mg II absorbers in the closest, non-overlapping redshift slice to the BR field — i.e., the field centred at $z = 0.682 \pm 0.060$ and corresponding to the usual BR field-of-view. Axes are labelled in pixels, where 1 pixel $= 4^2\,\mathrm{Mpc}^2$. S/N limits of: $4, 2$ and 4 were applied to the $\lambda_{2796}, \lambda_{2803}$ Mg II lines and quasar continuum, respectively (details of S/N cuts are discussed in section 3.1). The probes (quasars) responsible for the Mg II arising here have redshifts $z > 0.862$ so that they are the same probes responsible for the Mg II absorbers in the BR field centred on the usual redshift slice ($z = 0.802 \pm 0.060$). The figure shows that there are no filaments correlating to the BR indicating that the BR is not a result of artefacts in the probes.

investigate the second point by manually checking each of the quasar spectra that are probes to the Mg II absorbers in the GA that Anand21 missed. There were 16 from 51 absorbers that Anand21 missed, and none was due to the small fraction of removed quasars in DR16Q that was mentioned earlier. In each of the quasar spectra (corresponding to the GA) the Mg II doublets were visually confirmed, but the 16 absorbers missed by Anand21 had profiles that were generally complex, broad or weak. This again suggests that the Anand21 Mg II detection algorithm has a narrower detection window at the cost of losing some real absorbers. Conversely, the Z&M Mg II detection algorithm could conceivably contain more spurious absorbers while likely managing to detect a higher percentage of the real absorbers.

3 Statistical analysis

The discovery of the BR was made serendipitously when looking at the previously documented GA field with the Anand21 data. We now present the statistical analysis of the BR, taking a similar approach to the previous work in Lopez22. Given the nature of the discovery, the analysis is necessarily post-hoc. However, given the previous work presented in Lopez22 we

JCAP07(2024)055

are able to follow the guidelines set there, consequently alleviating many of the problems associated with post-hoc analysis.

Simulations are often advocated in contemporary astrophysics and cosmology, but we do not consider them likely to be effective or efficient here. Their complexity would be too great and would have too many unknowns and uncertainties. Consider, for example, that the simulations would have to incorporate: simulating the universe in general; the occurrence of quasars in that simulated universe; the observational parameters of the imaging and spectroscopic surveys and their on-sky variations; and the detection of the Mg II by software. Instead, we have taken the more practical approach of (i) using the data to correct the data, and (ii) seeking independent corroboration of features using independent tracers.

This section is divided in the following manner. (3.1) We assess the BR from a 'first look' perspective by using a heuristic process of stepping through redshift slices and determining the optimum redshift for the BR. (3.2) We use the Convex Hull of Member Spheres (CHMS) and the Minimal Spanning Tree (MST) significance calculations for assessing the significance of the BR. We apply these two methods of significance calculations to four sets of BR absorber-member estimates: the SLHC groups; the visually-identified BR absorbers (both including and excluding the inner absorbers); and the FilFinder-identified absorbers. (3.3) The 2D FilFinder algorithm is applied to the pixel image containing the BR to objectively identify filaments in the field. (3.4) Finally, we apply the 2D Cuzick and Edwards test to the BR field to determine the significance of clustering in the field (not the candidate structure itself).

3.1 Single-Linkage Hierarchical Clustering algorithm

The Single-Linkage Hierarchical Clustering (SLHC) algorithm is equivalent to a Minimal Spanning Tree (MST in a generic sense, not to be confused with the MST *significance* calculation in section 3.2) when separated at a specified linkage scale. Our particular application of the algorithm was first described in [12], in combination with the Convex Hull of Member Spheres (CHMS) algorithm which assesses the significance of a specified structure. The SLHC/CHMS method has been used to locate and assess LSS in both quasars and Mg II absorbers [2, 11, 12].

Previously, the inherent difficulties of the Mg II method have been discussed, especially in relation to applying statistics on an intrinsically inhomogeneous dataset. The quasars act as probes of the intervening matter, so the varying availability of background quasars leads to an incomplete image or map of the intervening matter, in this case, the Mg II absorbers. The inhomogeneity of the quasars, both intrinsic and of the survey, contribute in a complicated way to the inhomogeneity of the Mg II absorbers. Of course, with large data and large survey areas, approximations can be made. Before applying the SLHC algorithm we define the field-of-view (FOV) for the analysis presented here.

First, the BR appears in the north of the usual GA field, so we re-centre the Mg II images accordingly. Second, the field containing the BR is close to the northern SDSS footprint border as well as a southern border arising from much lower quasar coverage. We choose to shrink slightly the typical size of a Mg II image to avoid these areas. Third, given the generally patchy DR16Q quasars, and thus the corresponding Mg II absorbers in the Anand21 databases, we apply signal-to-noise (S/N) limits to the Mg II absorption lines and

JCAP07(2024)055

the continuum. We calculate the S/N of the Mg II lines by:

$$S/N = W_r/W_{\rm err}$$

where Wr is the equivalent width of the line, and $W_{\rm err}$ is the corresponding error in the Mg II line. For the continuum, Anand21 provide the median quasar S/N. Applying S/N limits has the effect of removing spurious and potentially false positive absorbers as well as generally reducing the patchiness in the data. Setting additional[2] limits to the magnitude of the quasars would also have a similar, desirable effect. However, not all quasars will have the same integration time, so faint quasars could have good S/N due to long exposures. Following the example by Z&M, we apply a S/N limit of 4 and 2 for the λ_{2796} and λ_{2803} lines respectively. Since the S/N of the quasar continuum necessarily has equal or higher S/N than the λ_{2796} line we apply a S/N limit to the quasar continuum of 6. Applying the condition of S/N $\geq$ 6 to the quasar continuum could be too restrictive, and later we will apply a less conservative condition to the continuum for comparison.

The CHMS significance is calculated by the rate of occurrence of volumes smaller than the CHMS volume of the structure by randomly distributing the absorbers belonging to the structure at a density equal to the control field density — the simulations are repeated 1000 times. Previously, the control field was chosen to be that of the field being assessed. However, this would mean that a percentage of the field absorbers are those belonging to the structures of interest, e.g., the GA and BR in the GA/BR FOV. In addition, the FOV containing the BR is small, so small-scale inhomogeneities have a much larger effect on the average density. Conversely, choosing a control field that is too large will lead to problems involving the large-scale inhomogeneities of the SDSS survey, explained above. Subsequently, we have designed two versions of control fields accounting for the northern portion of the SDSS footprint (overdense region) and the southern portion of the SDSS footprint (underdense). Each version can be chosen depending on the location of the field of interest. So here, we will be using version-1 of the control field — figure 5.

The SLHC is equivalent to an MST when separated at a specified linkage scale: thus the choice of linkage scale will determine the maximum distance between points that would be considered 'joined', or a candidate structure. The term 'structure'[3] here is not be confused with a gravitationally-bound system, but is instead referring to a grouping of more than 10 (a specified minimum) members (in this case, Mg II absorbers) that have an MST with distances smaller than the linkage scale. LSSs are not expected to be gravitationally bound, as, indeed, superclusters and great walls are not expected to be gravitationally bound. Similar usages and definitions of 'structure' are common in LSS studies [9, 10, 34, 35]. The candidate structures are then assessed by the CHMS to determine whether their volumes are statistically

[2]A base-line magnitude limit of $i <= 20.5$ is applied to the DR16Q quasars as part of the read-in process since the completeness declines steeply for fainter quasars.

[3]For a working definition, in investigating LSS, we often consider a candidate structure to be a set of N connected tracers, the containing volume of which is a $n\sigma$ departure from the containing volume expected for a uniform, random distribution. We might choose to consider further only those candidates for which the amplitude $n\sigma$ exceeds some threshold. 'Connected' and 'containing' volume will often be determined *algorithmically*; for both, there is an implicit assumption of a uniform host survey, which might be approximately true only in restricted areas.

JCAP07(2024)055

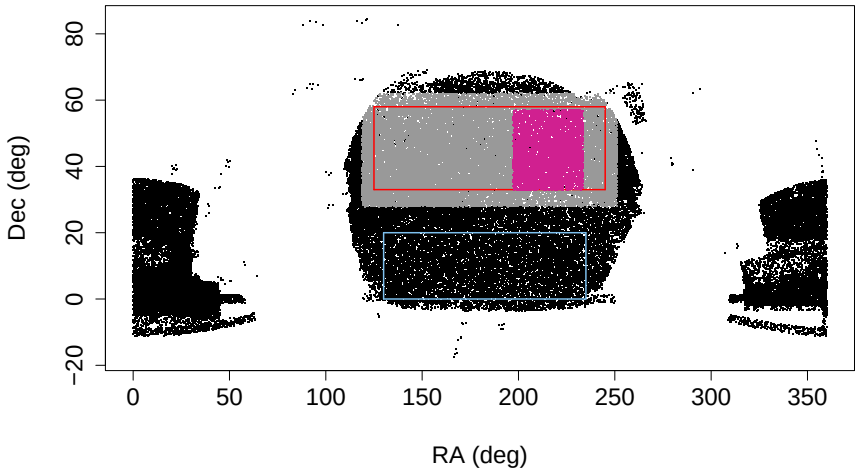

Figure 5. The SDSS DR16Q footprint. The grey points are the input quasars for the control field and the pink points correspond to the Mg II absorbers in the field of interest. The control fields are outlined by lines in red (overdense region, version-1) and blue (underdense region, version-2).

significant. In Lopez22 we discuss the effects of varying the linkage scale, so here we choose to scale the linkage scale according to the Mg II number density of the control field and the number density of the GA field — the GA field being the candidate field from which to scale all other fields, i.e.,

$$s = (\rho_0/\rho)^{1/3} s_0$$

where s and s_0 are the linkage scale for the control field and the GA field respectively, and similarly ρ and ρ_0 are the densities of the corresponding fields. The linkage scale is to be taken as a guideline; if the linkage scale is too small then potentially interesting candidate structures will be missed, and if the linkage scale is too high then too many points will be grouped as one seemingly coherent structure, but that would of course reflect in the CHMS significance. We find that the linkage scale set for the GA field (the field which we now use as the base-line) was an appropriate choice for the specific field density. However, we saw that even with the chosen linkage scale the SLHC algorithm identified the GA as two, individual, overlapping candidate structures. We reason that, when using a smaller linkage scale, candidate structures that are overlapping or adjacent could reasonably belong to the same structure. It is important to recognise that multiple candidate structures overlapping and adjacent to each other will still need to be assessed with the CHMS or MST significance, which would then objectively determine whether their agglomeration is statistically significant (remember, if the whole field was joined as one structure then this would of course not be statistically significant).

As with the GA analysis, we step through overlapping redshift slices and use the SLHC/CHMS algorithms to determine the redshift of the peak signal of the BR. Given the much larger Mg II database from Anand21, even after S/N limits are applied, it is expected that the field density containing the BR is much higher than the GA field in the Z&M databases, and therefore the chosen linkage scale will be correspondingly lower. The five redshift slices assessed are centred at: 0.682, 0.742, 0.802, 0.862 and 0.922, each with a redshift thickness of $\Delta z = 0.060$; the results are shown in table 1.

JCAP07(2024)055

Central redshift	**Linkage scale (Mpc)**	**No. candidate structures**	**No. candidate structures with $\sigma_{\mathrm{CHMS}} \geq 3.5\sigma$**	**Maximum σ_{CHMS} (σ)**	**Maximum Mg II absorber membership**
0.682	79.3	4	0	3.3	17
0.742	79.3	5	1	3.5	16
0.802	79.5	8	1	4.5	28
0.862	79.6	6	2	4.7	42
0.922	81.1	4	1	4.1	26

Table 1. Results from the SLHC/CHMS on five, overlapping redshift slices to determine the optimum redshift slice for the BR signal. The FOV of each redshift slice corresponds to the small, pink area seen in figure 5. S/N limits of $4, 2$ and 6 were applied to the $\lambda_{2796}, \lambda_{2803}$ Mg II lines and quasar continuum, respectively. All redshift slices have a thickness of $\Delta z = \pm 0.060$. The columns from left to right are: the central redshift of the field being assessed; the linkage scale used for the field being assessed, calculated as $s = (\rho_0/\rho)^{1/3} s_0$ (see the main text); the number of candidate structures identified in the field; the number of candidate structures identified in the field with a CHMS significance equal to or exceeding 3.5σ; the maximum CHMS significance calculated from the candidate structures; the maximum Mg II absorber membership identified from the candidate structures.

The BR that was originally identified visually appears almost fully (in a partly-open ring) in only the central redshift slice $z = 0.802$ indicating that this is the optimum redshift slice for the BR, as it was for the GA. (Note, the GA is also identified, and is statistically significant in the central redshift slice). The four structures contributing to the visually-identified BR are adjacent or overlapping on the sky, indicating that the separate structures plausibly belong to the same structure. The apparent splitting of a seemingly coherent structure was also seen with the GA, which was made up of two overlapping SLHC groups; the splitting of structures is an example of the limitations of applying the SLHC algorithm to an essentially incomplete dataset. Interestingly, the SLHC group corresponding to the bottom portion of the BR appears also to extend into the two higher redshift slices, $z = 0.862$ and $z = 0.922$, since there are similarly-shaped arcs (corresponding to the bottom portion of the BR) appearing at the same on-sky position in all three redshift slices ($z = 0.802, 0.862, 0.922$). (Note, the probes are not here restricted to be identical.)

As mentioned earlier, the condition of S/N ≥ 6 for the quasar continuum could be too restrictive. Anand21 calculate the S/N over the whole quasar continuum, rather than the local continuum at the point of an absorber. Therefore, the whole quasar continuum could have lower S/N overall compared with local S/N at the position of an absorber. Accordingly, we slightly relax the S/N conditions to $4, 2, 4$ for the $\lambda_{2796}, \lambda_{2803}$ Mg II lines and quasar continuum, respectively and repeat the above described analysis (see table 2).

We see again that the full BR is detected — this time a full, closed ring, and with the inclusion of the inner filament — in the central redshift slice $z = 0.802 \pm 0.060$, figure 6. The BR is located north of the centre point, spanning ~ 10 degrees in the RA and Dec axes (x and y axes respectively), and is made up of a collection of five structures identified by the SLHC algorithm.

JCAP07(2024)055

Central redshift	**Linkage scale (Mpc)**	**No. candidate structures**	**No. candidate structures with $\sigma_{\mathrm{CHMS}} \geq 3.5\sigma$**	**Maximum σ_{CHMS} (σ)**	**Maximum Mg II absorber membership**
0.682	76.7	6	0	3.2	16
0.742	76.2	7	0	3.3	19
0.802	75.8	10	1	4.1	30
0.862	75.7	7	1	3.7	27
0.922	77.1	6	0	3.4	15

Table 2. As with table 1. Slightly relaxed S/N limits of $4, 2, 4$ were applied to the $\lambda_{2796}, \lambda_{2803}$ Mg II lines and quasar continuum, respectively. All redshift slices have a thickness of $\Delta z = \pm 0.060$. The columns from left to right are: the central redshift of the field being assessed; the linkage scale used for the field being assessed, calculated as $s = (\rho_0/\rho)^{1/3} s_0$ (see the main text); the number of candidate structures identified in the field; the number of candidate structures identified in the field with a CHMS significance equal to or exceeding 3.5σ; the maximum CHMS significance calculated from the candidate structures; the maximum Mg II absorber membership identified from the candidate structures.

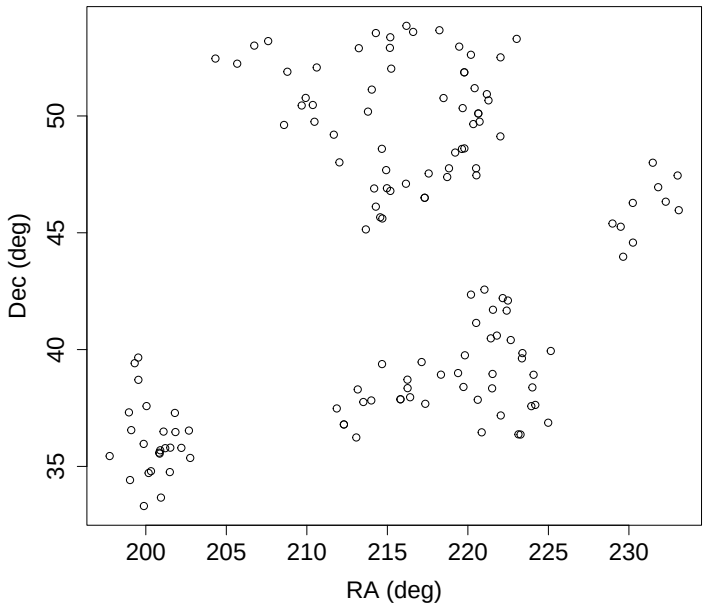

Figure 6. All the Mg II absorbers belonging to a candidate structure identified by the SLHC algorithm from results-2 in the redshift slice centred at $z = 0.802 \pm 0.060$. The field-of-view seen here corresponds to the pink points in figure 5. S/N limits of: $4, 2, 4$ were applied to the $\lambda_{2796}, \lambda_{2803}$ Mg II lines and quasar continuum, respectively. The BR can been seen to the north of the centre point. The visually-identified BR is seen here with an additional extension heading towards to the north-west direction, and the visually-identified inner filament is the central line cutting through the BR here. The BR spans ~ 10 degrees in RA and Dec coordinates. The large structure south of the BR belongs to the previously identified GA.

JCAP07(2024)055

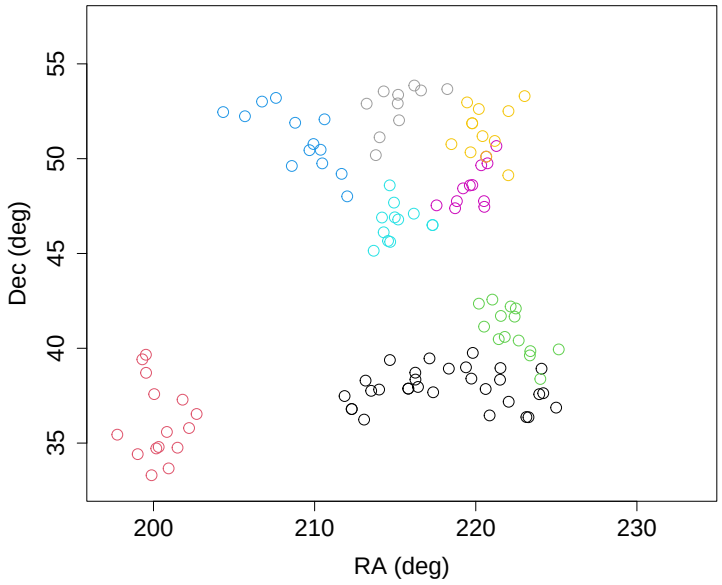

Figure 7. Eight of the 10 highest membership candidate structures identified by the SLHC/CHMS algorithms from results-2 in the redshift slice centred at $z = 0.802 \pm 0.060$. The colours represent the memberships which are ordered from high to low in the following way: black, red, green, blue, turquoise, pink, yellow, grey. The field-of-view here corresponds to the pink points in figure 5. The BR and inner filament are detected, but separated into five structures, that can visually be seen adjacent to each other or overlapping. In this figure, only the black points, representing absorbers belonging to the GA, are statistically significant.

Note the very high similarity of the two tables of SLHC/CHMS results (tables 1 and 2), where the only change is reducing the S/N limit of the quasar continuum from 6 to 4. For convenience, the first set of results with the more restrictive S/N limits will be referred to by MST results-1, and the second set of results with the less restrictive S/N limits will be referred to by MST results-2. We deduce that setting restrictive S/N limits (> 4) to the quasar continuum, after already applying S/N limits to the Mg II lines, is not absolutely essential, and possibly adds to the incompleteness of data in a detrimental way. An overview of the results is as follows. (1) In the two lowest redshift slices, in MST results-1 and results-2, there is only one statistically-significant ($> 3.5\sigma$) structure detected in total. The statistically-significant structure belongs to the redshift slice centred at $z = 0.742 \pm 0.060$ from results-1; it is a small group of absorbers located at the lower l.h.s. of the Mg II image, and of no relevance to the BR. In addition, other than a possibility of a thin filament forming in the Mg II image in the redshift slice centred at $z = 0.742$, there is no strong indication or detection of the BR in the two lowest redshift slices. (2) In the central redshift slice, $z = 0.802$, both results-1 and results-2 find one significant structure corresponding to the GA. The BR is separated into four and five (respective to results-1 and results-2) individual, adjacent or overlapping, structures, that are statistically insignificant on their own (see figure 7).

We could again be seeing here limitations of the Mg II method, as was seen with the GA, since the individual structures are overlapping or adjacent. In results-2, the visually-identified BR and inner filament absorbers are mostly detected (46 out of 59 absorbers, 78%) and form

JCAP07(2024)055

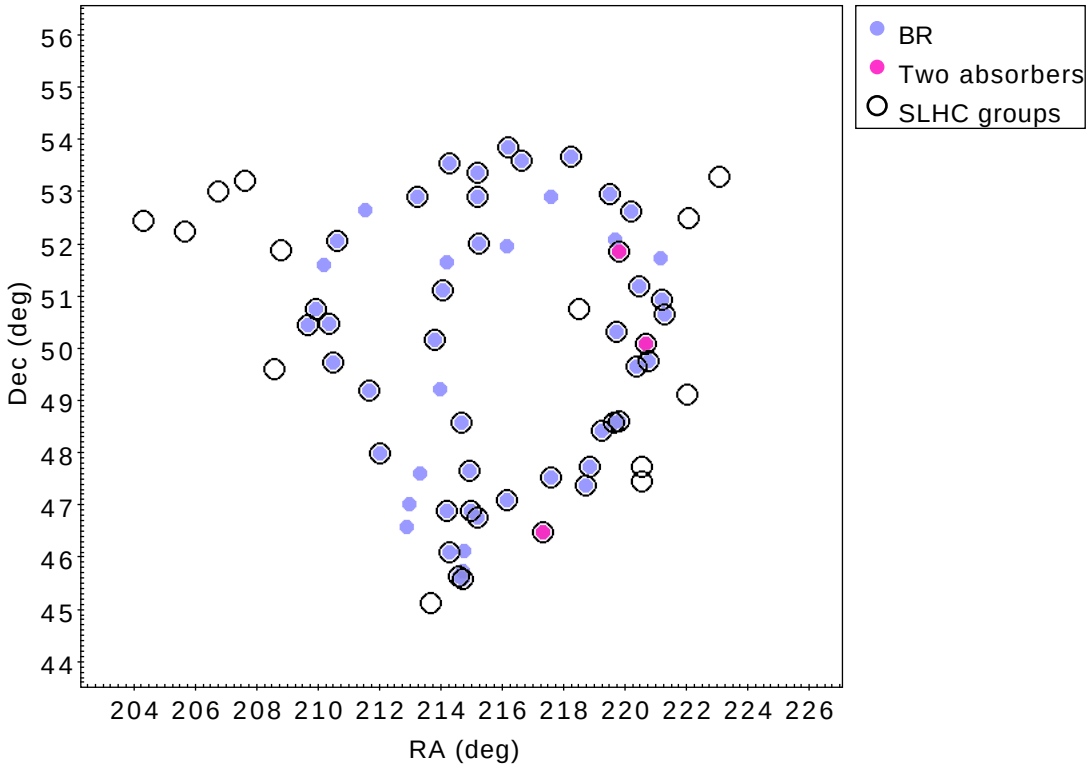

Figure 8. The visually-identified BR absorbers (lilac) and the SLHC-identified absorbers belonging to the 5 candidate structures from results-2 at $z = 0.802 \pm 0.060$ (black circles) that correspond to the visually-identified BR. The pink points indicate the positions where there are two absorbers occurring in a single spectrum. There are 46 out of 59 absorbers in common to the SLHC-identified and visually-identified BR and inner filament absorbers. Of the 13 absorbers in the visually-identified BR and inner filament absorbers that were not connected by the SLHC algorithm, 9 of these occur at the most extreme edges of the redshift range, possibly explaining their exclusion.

the full BR shape (see figure 8). (3) In the two highest redshift slices there are totals of 3 and 1 significant structures from MST results-1 and results-2 respectively. For results-1 the most significant structure in both redshift slices is an arc corresponding to the lower portion of the BR (see figure 9).

However, in results-2, we find the same arc that was detected in results-1, but over multiple structures, highlighting again the nuances of applying the SLHC algorithm to an essentially incomplete dataset. To clarify this, reducing the S/N limits in the quasar continuum from 6 to 4 initially appears inconsequential — i.e., their Mg II images appear on the whole unchanged and there is only a 15% increase of absorbers in the whole field from results-1 to results-2. But, when the SLHC algorithm is applied, then this small increase in absorbers increases the density-scaled linkage scale thus creating more broken structures. We scale the linkage scale of the SLHC algorithm to the density for a general approach to the wide-varying densities in the dataset (mostly due to survey bias). We can see that the absorbers identified as candidate structures corresponding to the arc in the redshift slice $z = 0.862 \pm 0.060$ in results-2 are very similar to the absorbers identified as one candidate structure in results-1. To further clarify this point, compare figure 9 with figure 10, and

JCAP07(2024)055

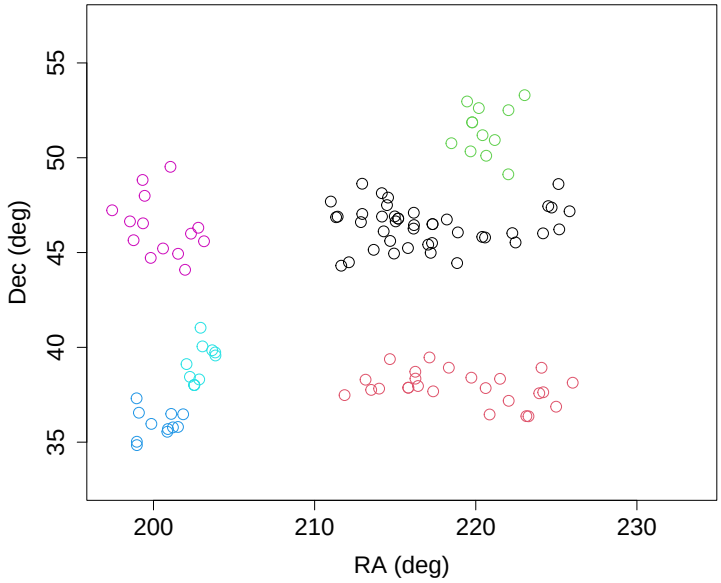

Figure 9. The 6 candidate structures identified by the SLHC algorithm from results-1 in the redshift slice centred at $z = 0.862 \pm 0.060$. The different colours represent the significances, and are ordered from high to low in the following way: black, red, green, blue, turquoise, pink. The two most significant structures belong to the BR and GA respectively, both which are also statistically significant.

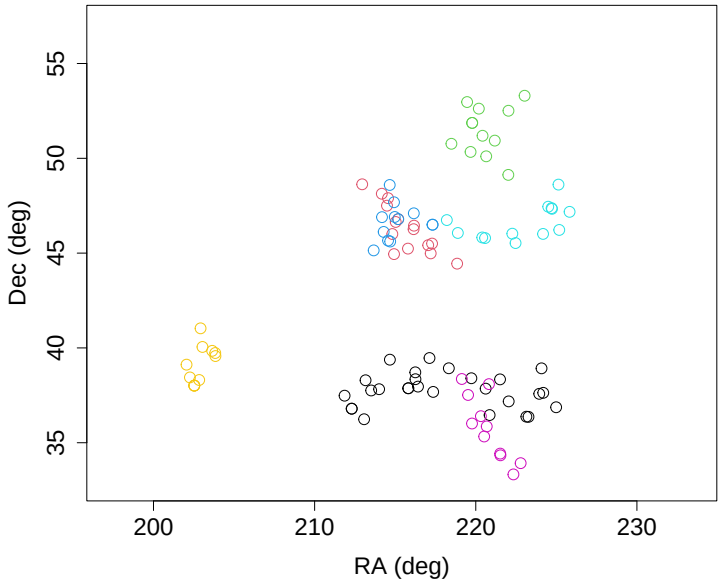

Figure 10. The 7 candidate structures identified by the SLHC algorithm from results-2 in the redshift slice centred at $z = 0.862 \pm 0.060$. The different colours represent the significances, and are ordered from high to low in the following way: black, red, green, blue, turquoise, pink, yellow. The absorbers belonging to the GA are statistically significant, shown in black. By comparing this figure with figure 9 we can see that the absorbers identified by the 3 individual, overlapping or adjacent structures, coloured red, blue and turquoise, are clearly the same absorbers identified by *one* full, statistically-significant structure that was found in results-1, highlighting the complications of applying the SLHC algorithm to an essentially incomplete dataset.

JCAP07(2024)055

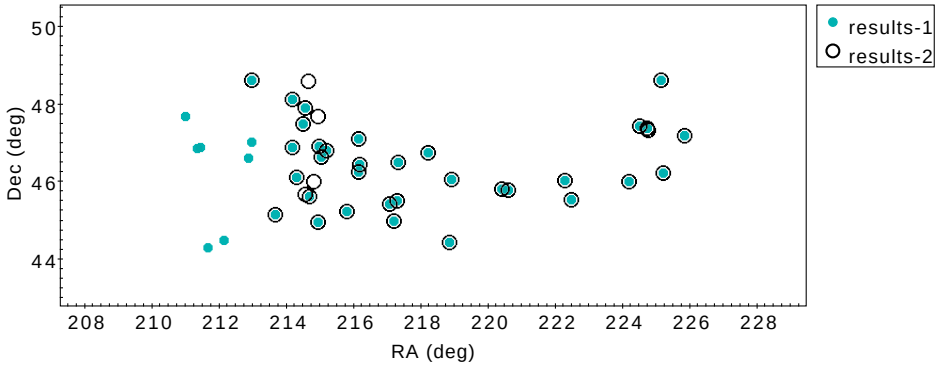

Figure 11. Mg II absorbers in the redshift slice $z = 0.862 \pm 0.060$ belonging to the arc identified by the SLHC algorithm as one, full, candidate structure from results-1 (turquoise) and as three, overlapping or adjacent, candidate structures from results-2 (black circles). There are 42 absorbers belonging to results-1, four of which appear as multiples per probe in two quasars, and 40 absorbers belonging to results-2, the same four of which appear as multiples per probe in two quasars. Both results connect many of the same absorbers, but in results-1, where the linkage scale is higher, there are additional absorbers connected by the SLHC algorithm all appearing on the l.h.s. of the arc. The additional absorbers in results-2 occur in the middle of the arc, and there are much fewer additional absorbers than for results-1, suggesting that these absorbers were identified due to the lowered restriction on the S/N on the continuum.

see also figure 11. There are 42 absorbers in the SLHC-identified arc in the redshift slice $z = 0.862 \pm 0.060$ from results-1 represented by the black points in figure 9, and a combined total of 40 absorbers in the three SLHC-identified candidate structures corresponding to the arc in the redshift slice $z = 0.862 \pm 0.060$ from results-2 represented by the red, blue and turquoise points in figure 10. 35 of these absorbers from results-1 and results-2 are in common to both results, confirming that the SLHC identified a high fraction (67% overlap) of the same absorbers between the two results. In fact, all 7 of the additional absorbers connected by results-1 all occur on the l.h.s. of the arc, indicating that the increased linkage scale in results-1 (due to lower field density) is only *extending* the arc, and not responsible for the central components of the arc. Due to the above, we reason that individual, SLHC-identified candidate structures that are overlapping or adjacent could reasonably be connected as one structure if given a more complete dataset.

In conclusion, the BR appears most obvious in the original, central redshift slice, $z = 0.802 \pm 0.060$, both visually and by the presence of individual SLHC structures overlapping or adjacent on the sky that comprise the visually-identified BR. The strongly, detected arc corresponding to the lower portion of the BR detected in a slightly higher redshift slice ($z = 0.862 \pm 0.060$) is also of particular interest in relation to the BR+GA system.

3.2 Significance: CHMS and MST

The CHMS and MST significance calculations are applied to: the SLHC-identified absorbers; the visually-identified absorbers; and the FilFinder-identified absorbers. In addition, the Alpha Hull algorithm is applied to the visually-identified absorbers for an estimate of the volume, overdensity and significance using simple Poisson statistics.

JCAP07(2024)055

	No. Mg II absorber members	CHMS signif.	MST signif.
BR only	51	3.3	4.0
BR all	62	5.2	4.1

Table 3. The CHMS and MST significances for the BR-all and BR-only absorbers. The CHMS significance is dependent on the volume and number of absorbers so, clearly, removing the inner absorber members and keeping the volume the same will reduce the CHMS significance. However, for the MST significance, the volume is not directly related, but instead it is related to the MST mean edge lengths. This is clearly shown in the results as the MST significance stays mostly the same, at $\sim 4\sigma$, and the CHMS significance decreases from 5.2σ to 3.3σ by excluding the absorbers enveloped by the BR.

3.2.1 SLHC-identified Mg II absorbers

To determine the significance of the BR in its entirety, we take the SLHC-identified absorbers from results-2 that make up the BR (i.e., the BR in figure 6), and apply the CHMS algorithm. Remember that the CHMS has the ability to assess the significance of a structure by comparing the observed convex-hull volume with the volumes that would be expected for a set of random distributions of those same absorbers at the control density of absorbers for the same redshift interval. Based on the definition of the CHMS volume and significance calculation, the algorithm is optimal when applied to clumpy structures, with no obvious gaps, holes or curvature that would lead to an overestimation of the volume. Clearly, this is not the case with the BR, having a large volume mostly unoccupied by absorbers in its centre. Instead, the MST-significance calculation introduced by [36] could be more appropriate, which uses the mean MST edge-length between neighbouring data points. Using both methods we then find that the SLHC-identified BR in its entirety has a CHMS significance of 3.6σ, and an MST significance of 4.7σ. Both tests indicate statistical significance, but we can see that CHMS has likely overestimated the BR volume leading to a much lower significance compared with the MST-significance test.

3.2.2 Visually-identified Mg II absorbers

We then take the visually selected absorbers of the BR, and everything within the BR, for which there are a total of 62 absorbers (see figure 2), and apply the CHMS to these absorbers only. The CHMS algorithm then calculates a significance of 5.2σ. The significance calculated here is likely the upper limit estimate for the BR, as the algorithm was applied to those absorbers that were visually-selected. We can similarly repeat this work for the BR-only absorbers, as well as compare the MST significance with the CHMS significance. Clearly, removing the BR innards will reduce the significance calculations for the CHMS, since the volume will remain the same but the number of absorbers will be reduced. In contrast, for the MST significance, the mean MST edge length may not be greatly affected by removing the BR innards, as seen in table 3. We find that on both occasions, using the BR-all and BR-only absorbers, the MST significance is roughly the same, at $\sim 4\sigma$. In contrast, for the CHMS calculation, the significance drops from 5.2σ to 3.3σ after removing the absorbers

JCAP07(2024)055

contained within the BR. However, even after removing all of the BR inner absorbers the CHMS significance is still greater than 3.0σ, but not quite reaching 3.5σ which is the usual standard we apply for comparing structures. Of course, the CHMS calculation on the BR-*only* absorbers gives a drastic under-representation of the true significance since we have forcefully removed absorbers contained within the BR while keeping the unique volume the same.

For comparison, we can estimate the volume of the BR using the 2D Alpha Hull algorithm. First, the Alpha Hull area of the BR is repeatedly calculated 500 times from the BR by drawing a cloud of points in a circle with radius equal to half the mean MST edge length around each of the Mg II absorbers in the BR. Then, the area is multiplied by the physical size of the redshift range of the BR absorber members. In this manner, we are calculating the volume of a somewhat cylindrical, tube shape. The benefits of this method versus the CHMS is that we can eliminate the central region of the BR where there are very few absorbers. The downside of this method is that, although the absorbers on the sky make up a ring shape, we later see that the 3D distribution of the absorbers is more of a coil shape, so we are again overestimating the volume of the BR (and underestimating the overdensity and significance of the structure). Nevertheless, using this method we obtain a volume of $21.8 \times 10^6\,\mathrm{Mpc}^3$, an overdensity of 0.75 and a significance of 4.0σ for the number of absorbers in this volume based on Poisson statistics. The significance calculated from the Alpha Hull here, although simple, agrees with the MST-significances of the SLHC-identified absorbers and the visually-identified absorbers, which adds further confidence to the statistical assessment of this structure.

3.2.3 FilFinder-identified Mg II absorbers

Finally, we have seen the CHMS algorithm as well as the MST significance test applied to the SLHC-identified and visually-identified absorbers, so now we will apply both algorithms to the FilFinder-identified absorbers. The FilFinder work is discussed next, in section 3.3, and we are referencing figure 13(d) for the work in this section. The FilFinder algorithm is applied to 2D pixel images, so the physical absorber points are irrelevant to the algorithm, but we can estimate the absorbers identified by the filament by including those that are attached to the filament in the figure. Our estimation of the absorbers connected by the FilFinder algorithm is shown in figure 12. We can intuitively see that a volume containing all of the FilFinder-identified absorbers will include many large, empty sub-volumes — e.g., the centre of the BR and the volume between the 'extended filaments' connected to the BR. The BR volume was also overestimated with all previous identifications of the BR, which can be confirmed with the comparison of, in particular, the BR-all with the BR-only absorbers, and the CHMS with the MST significances. So, when the CHMS algorithm is applied to the FilFinder-identified absorbers, it calculates a 2.5σ significance. In contrast, the MST-significance test estimates that the FilFinder-identified absorbers have a significance of 3.6σ, which is generally in agreement with all previous estimates of the BR significance using the MST calculation and the Alpha Hull Poisson statistics. So, again, the BR volume is considerably overestimated, this time using the FilFinder-identified absorbers, and the CHMS significance is therefore underestimated as a consequence, which can be confirmed with the use of the MST-significance test.

JCAP07(2024)055

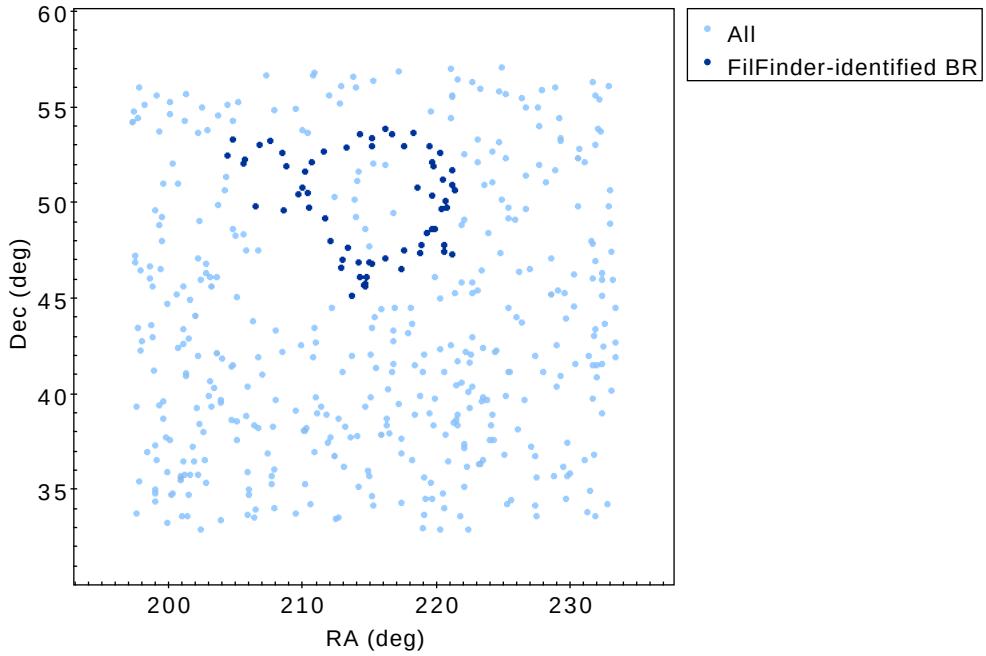

Figure 12. The Mg II absorbers belonging to the whole BR field, represented by light blue points, and the FilFinder-identified BR absorbers represented by dark blue points.

	SLHC	Visual BR-all	Visual BR-only	FilFinder
CHMS	3.6	5.2	3.3	2.5
MST	4.7	4.1	4.0	3.6

Table 4. The CHMS and MST significances of the BR calculated for each set of identified absorbers (SLHC, visual BR-all, visual BR-only and FilFinder).

3.2.4 Summary of significances

We have shown our application of the CHMS and MST significance calculations to four sets of uniquely-identified BR absorber members. Table 4 summarises all of the above significance calculations. The results are: the total mean significance of the BR (all results from table 4 considered) is $(3.88 \pm 0.83)\sigma$; the mean CHMS-significance is $(3.65 \pm 1.13)\sigma$; and the mean MST-significance is $(4.10 \pm 0.45)\sigma$. From these results we can see that the variation of the CHMS-significance is a considerable fraction of the average, indicating its results are to be taken with caution. On the other hand, the MST-significance has much lower spread, indicating that for the purpose of analysing the BR, the MST-significance test may be more appropriate, given the difficulty of defining a volume around a ring-like structure without incorporating overestimations of the volume (as is the case with the CHMS algorithm).

3.3 Filament identification algorithm

FilFinder is a filament identification algorithm created by [37]. It uses mathematical morphology to identify filaments ranging in size, shape and brightness on a 2D pixel image. The

JCAP07(2024)055

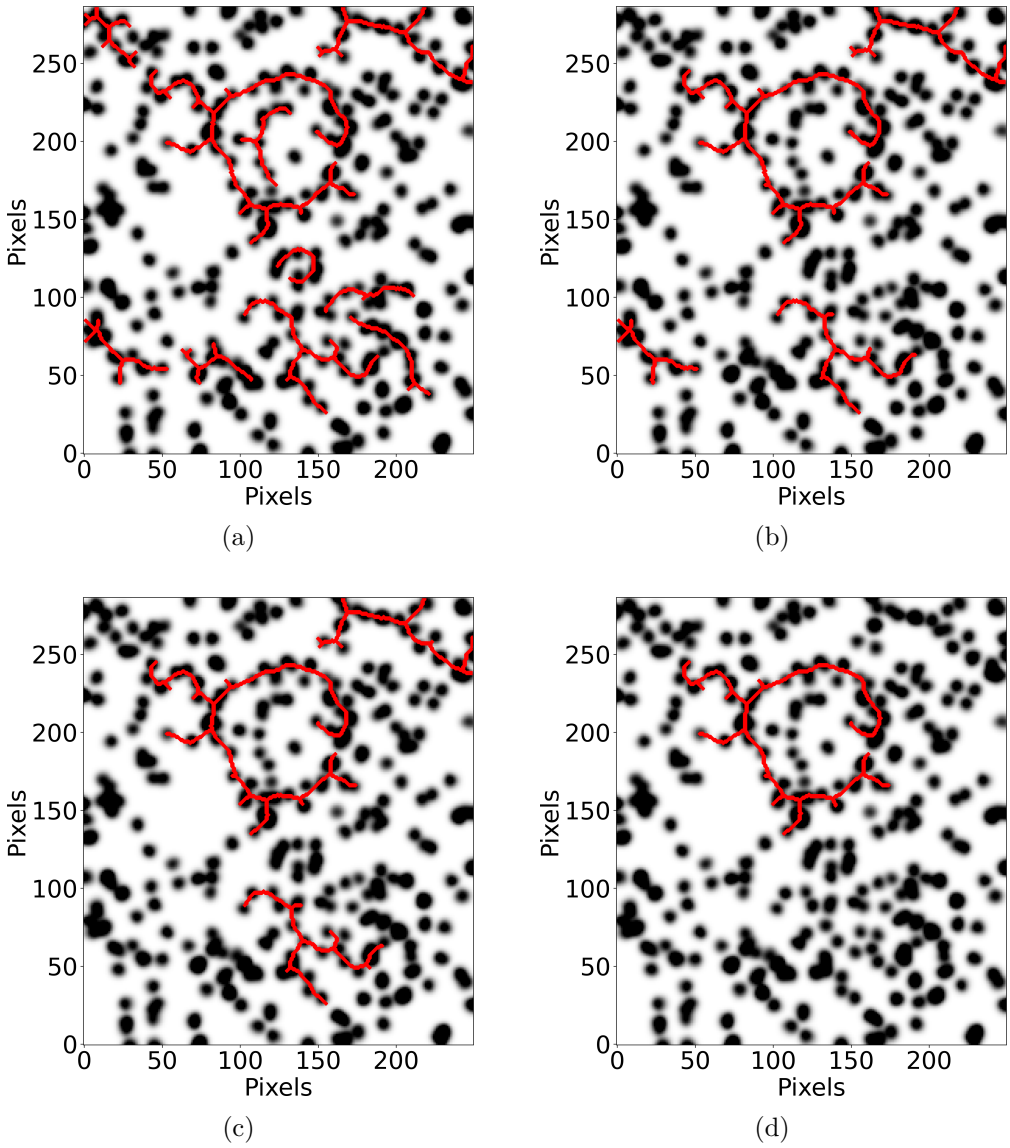

Figure 13. Applying the FilFinder algorithm to the standard BR field and increasing the size threshold incrementally to show the elimination process of small filaments. All axes are labelled in pixels, where 1 pixel = 4^2 Mpc^2. (a) The standard parameters, for which adaptive threshold is 18 pixels, smooth size is 12 pixels, and size threshold is 576 pixels. For the remaining figures we incrementally increase the size threshold. (b) Size threshold is 800 pixels. (c) Size threshold is 1000 pixels. (d) Size threshold is 2000 pixels.

algorithm was intended for use in small (10^1–10^3 pc), gaseous areas, such as star formation regions and the interstellar medium [38–40]. So, applying it to cosmological LSS is new, and we have had to make adaptations in the parameter settings to suit the data. We use the following input parameter settings. (1) Adaptive threshold — the expected width of a typical filament. We choose a value (in number of pixels) equivalent to a filament that is only one absorber wide. Since the Mg II absorbers in the Mg II images span a diameter of approximately 12 pixels, the adaptive threshold is set to 12. (2) Smooth size — scale on

JCAP07(2024)055

which to smooth the data. Our data is already smoothed and flat-fielded, so it is possibly unnecessary to smooth beyond the size of a Mg II absorber: i.e., we shall implement a smoothing size that does not affect the already smoothed Mg II absorbers. Therefore, we set smooth size to a value of 12 pixels. (3) Size threshold — the smallest area to be considered a filament. Using again the estimated value for the number of pixels across a single Mg II absorber, we set this value at $4 \times 12^2 = 576$ pixels. That is, the minimum area to be considered a filament is made up of 4 Mg II absorbers (with the absorbers imagined as squares rather than as circles, for simplicity).

We use the FilFinder package available in Python to objectively identify the filaments present in the BR field. For the above parameters we find that there are no visually-obvious consequences for relatively small changes (e.g., within a few percent of the chosen value). However, much larger changes in the parameter choices render noticeably different, and consequential, results. For this reason we experiment with changing the standard parameter values above to gain a better understanding of the FilFinder algorithm when applied to cosmological data. The FilFinder algorithm is applied multiple times, with different parameter settings, on the Mg II image containing the BR (figure 1), and the results are discussed below.

First, the adaptive threshold and smoothing size are related in a way that increasing one has an almost indistinguishable effect from decreasing the other, for reasonable values (e.g., < 40 pixels, since larger values flag a warning within the FilFinder algorithm). More specifically, the most meaningful and interesting effects can be found when one focuses on the ratio between the values. This can be understood intuitively since smoothing size is the scale on which to smooth the filaments and adaptive threshold is the typical width of those filaments, the size of which is affected by the smoothing size. When the adaptive threshold and smoothing size ratio is $1:2$ there is an undesirable effect of creating 'blurred' masking borders over the filaments; this is when the borders of the mask around individual filaments overlap. However, the opposite is true when the adaptive threshold and smoothing size ratio is $2:1$, which has the effect of creating more concise borders around the filaments, but it also drastically reduces the number of filaments that can be detected. With this in mind, we choose to slightly increase the adaptive threshold from 12, a single Mg II absorber, to 18, 1.5 times a Mg II absorber, while keeping the smoothing size at 12 as usual, thus creating a ratio of $3:2$ for the adaptive threshold and smooth size.

Secondly, the size threshold simply determines the minimum size to be considered a filament. Increasing the size threshold incrementally and comparing results demonstrates the elimination process of small filaments. So now using the updated parameter values, where the adaptive threshold is set at 18 pixels and the smoothing size is kept at 12 pixels, we incrementally increase the size threshold and show the filaments that survive the elimination process (see figure 13). Immediately it becomes clear that the BR is the largest, and most dense, filament in the field. The BR filament is the only filament left with the largest size threshold limit. In fact, the BR is not eliminated until the size threshold exceeds 4200 pixels. Using the elimination process with the FilFinder algorithm has given an impressive indication for the size and uniqueness of the BR compared with the rest of the field.

Next, we apply the same method of analysis to the SDSS DR16Q quasars in the same field and the same redshift slice as the Mg II absorbers containing the BR for comparison

JCAP07(2024)055

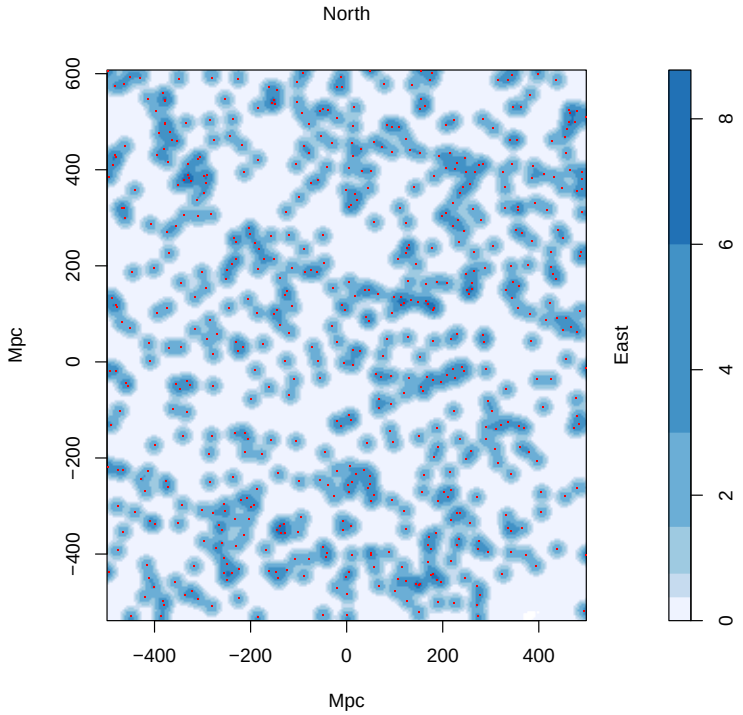

Figure 14. The tangent-plane distribution of quasars in the redshift slice $z = 0.802 \pm 0.060$. The blue contours, increasing by a factor of two, represent the density distribution of the field quasars which have been smoothed using a Gaussian kernel of $\sigma = 11$ Mpc. Magnitude limits have been applied to the quasars such that $i \leq 20.0$. The field-of-view corresponds to the small, pink area seen in figure 5. There is no strikingly obvious structure by eye, but when the FilFinder algorithm is applied to this field it can detect a filamentary ring-like shape that coincides with the BR.

with an independent data source. We want to reduce the noise of the high number density of quasars so we apply an i-magnitude (i) limit of $i \leq 20.0$, such that only the intrinsically very bright quasars are included. The field size and redshift interval for producing the quasar image is the same as that for the Mg II absorbers from figure 1: that is, the quasars are chosen to be those that lie in the same field as Mg II absorbers, not to be confused with the background quasars responsible for the Mg II absorbers. The quasar image is seen in figure 14. The FilFinder algorithm is applied to the quasar image in the same manner as described above with the Mg II absorbers, with the following parameter settings: adaptive threshold = 18, smoothing size = 12 and size threshold = 576 (see figure 15(a)). Given the much higher density of the field quasars compared with the Mg II absorbers, even after i magnitude cuts have been made, we can see that there are generally more filaments identified (figure 15(a)). Incrementally increasing the size threshold will remove the small filaments and leave only those able to survive the cuts — so just the large filaments of interest. Figures 15(a)–15(d) show the results from FilFinder applied to the field quasars with increasing size threshold.

When the FilFinder algorithm is applied to the field quasars, and the size threshold is incrementally increased, we are left with only a ring-like filament that coincides with the BR. This is particularly interesting as it demonstrates from independent corroboration that the quasars also follow a similar shape to the Mg II absorbers. We can also visualise

JCAP07(2024)055

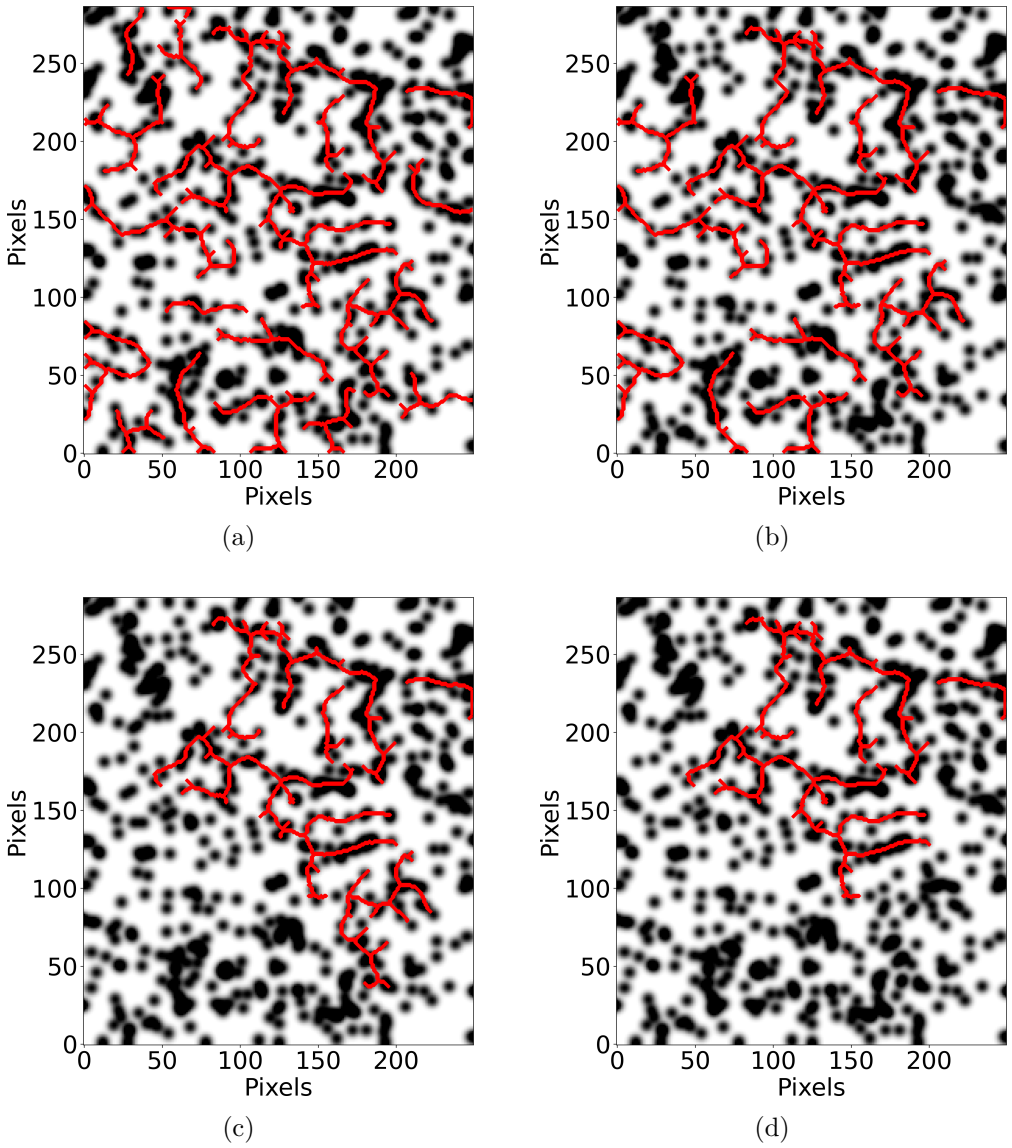

Figure 15. Applying the FilFinder algorithm to the field quasars corresponding to the standard BR field and incrementally increasing the size threshold to show the elimination process of small filaments. All axes are labelled in pixels, where 1 pixel = 4^2 Mpc^2. (a) Using the standard FilFinder parameters where adaptive threshold is 18 pixels, smooth size is 12 pixels, and size threshold is 576 pixels. For the remaining figures we incrementally increase the size threshold. (b) Size threshold is 1000 pixels. (c) Size threshold is 2000 pixels. (d) Size threshold is 4000 pixels.

the relationship of the Mg II absorbers with the bright field quasars by superimposing the quasar image onto the Mg II image (see figure 16). In section 4.1 we further investigate the observational properties of both field quasars and DESI clusters in the BR field.

3.4 Cuzick and Edwards test

The Cuzick-Edwards (CE) test [47] was created to assess the clustering of cases in an inhomogeneous population. It is a 2D, case-control statistical method that deals with variations in spatial populations. This method has shown to be useful for the particular data

JCAP07(2024)055

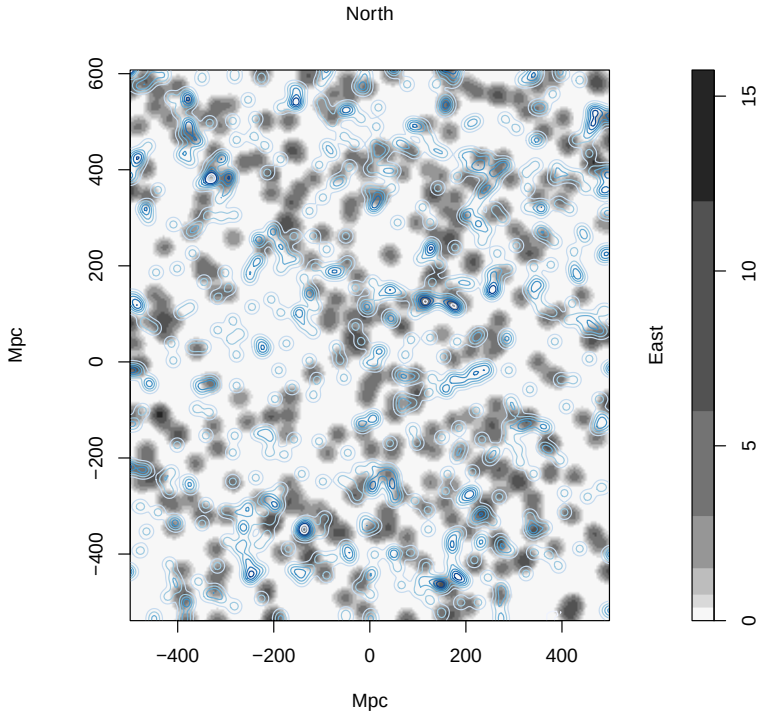

Figure 16. The tangent-plane distribution of Mg II absorbers in the redshift slice $z = 0.802 \pm 0.060$ superimposed with the tangent-plane distribution of quasar positions in the same redshift slice (not to be confused with the background probes). The grey contours, increasing by a factor of two, represent the density distribution of the absorbers which have been smoothed using a Gaussian kernel of $\sigma = 11$ Mpc, and flat-fielded with respect to the distribution of background probes (quasars). The blue contours, increasing by a factor of two, represent the density distribution of the field quasars which have been smoothed using a Gaussian kernel of $\sigma = 11$ Mpc. In the Mg II image, S/N limits of 4, 2 and 4 were applied to the $\lambda_{2796}, \lambda_{2803}$ Mg II lines and quasar continuum, respectively. In the quasar image, magnitude limits were applied such that $i \leq 20.0$. In general, we find that the blue contours follow the grey contours.

that we are working with; the Mg II are the cases to be assessed, which are affected by the inhomogeneous spatial distribution of the background probes (quasars). This method assesses the statistical significance of clustering by assessing the occurrence of cases within the k nearest neighbours, but it cannot, however, assess the significance of individual candidate structures. Therefore, it is a useful additional method to analyse the field containing the BR.

The CE test was first applied to cosmological (and to our knowledge, astrophysical) data when analysing the GA (section 2.3.3 in Lopez22); before this, the method had mainly been used in the context of medical research (e.g. for patterns in diseases across varying population sizes). We can now follow the steps and process presented in Lopez22 for the BR. (We are using the application *qnn.test* in the R package SMACPOD by [48].)

As mentioned previously in Lopez22, the power of the CE test is affected by the control-case ratio, and a ratio between 4 and 6 is found to be optimal [47]. For this reason, we continue to use a control-case (i.e., probes to absorbers) ratio of 5 : 1, which, for the BR field, requires removing $\sim 90\%$ of the probes. The $\sim 10\%$ remaining probes are randomly selected for each of the 200 runs of the *qnn.test*, which itself is computed for 499 simulations (the default setting).

JCAP07(2024)055

We begin by assessing the BR field, and then we successively shrink the FOV to 'zoom in' on the BR, which is presumably the main feature contributing to any clustering patterns detected in the field. Unlike the GA, the BR is a full ring shape, so the successive zooming is limited in both axes. Therefore, we apply only two successive zooms to the BR, beyond which the BR would extend beyond the FOV. We then apply the CE test on four other fields that are unrelated and detached from the BR field, for comparison with the BR field. The four unrelated fields are chosen to be at the same redshift as the BR field ($z = 0.802 \pm 0.060$), the same field size (equivalent to the second 'zoom' of the BR field) and the same declination ($\delta = 50°$), so that the only change from the BR field to the unrelated fields is to move the right ascension (RA) centre point — the unrelated fields are then outside the BR field but within version-1 of the control area (see figure 5). For the BR field, we repeat the CE test (with 200 runs and 499 simulations) 10 times altogether to investigate how the random selection of probes (controls) could affect the CE statistics. The distribution of p-values calculated from applying the CE test to the BR field indicates tentative significant clustering ($p \leq 0.05$) for a range of chosen q (k) values. The median p-value dropped to a minimum of $p = 0.0238 \pm 0.0015$ over the 10 repetitions of the CE test at $q = 61$, corresponding to a significance of 2.0σ. However, in the four other unrelated fields there was no (with the exception of exactly two data points) significant (significant is here defined as $p \leq 0.05$) clustering detected, suggesting that the clustering seen in the BR field is special (see figure 17) — as was similarly found with the GA previously. In one of the unrelated fields there were two points, at $q = 2$ and $q = 8$, where the median p-value dropped below the $p = 0.05$ threshold, which is here considered tentative significant clustering. However, since it was at a much lower q value, the CE test was likely here detecting very small-scale clustering, and not related to the same type of clustering seen in the BR (and GA) field. Overall, the clustering seen in the BR field mimicked the clustering that was also seen in the GA field, but here at a tentative ($p \leq 0.05$) significance level; the clustering in the BR field was inconclusive at the $\sigma > 3.0$ significance level.

4 Observational properties

4.1 Corroboration with independent data

Earlier, in section 3.3, we saw that the bright field quasars have identified filaments similar to those of the Mg II absorbers. It was also shown that there is a plausible visual association of the field quasars and Mg II absorbers from superimposing the contour maps of each dataset (figure 16). We can continue to use the contour maps from the quasars, and now also the DESI clusters [49], looking at a larger FOV, and investigate the visual association of the independent datasets with the MgII absorbers on a larger scale (see figure 18).

The visual investigation of quasars and DESI clusters with Mg II absorbers indicates that generally there is plausible association of both independent datasets with the absorbers. The association can be seen clearly when comparing the 'voids' in the data; where there are no absorbers there tend also not to be very many quasars or DESI clusters. The visually most striking association is seen in figure 18(d) where the green contours of the DESI clusters seem to follow the same filamentary trajectory as the Mg II absorbers in many cases. Interestingly,

JCAP07(2024)055

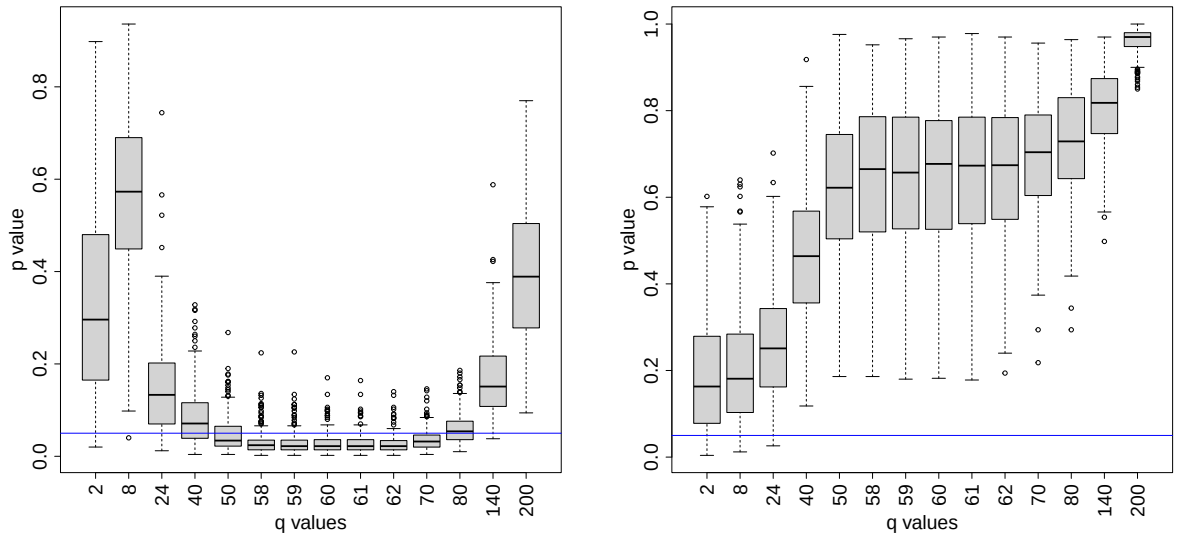

(a) (b)

Figure 17. The Cuzick and Edwards (CE) test applied to the second 'zoom' of the BR field and an unrelated field (a and b respectively) for comparison. The figures show a box-plot of the distribution of p-values over 200 runs of 499 simulations as a function of chosen q (k) value. (a) The BR field shows tentative significant clustering ($p \leq 0.05$) between $q = 50$ and $q = 70$, reaching a minimum of $p = 0.022$ between 59 and $q = 62$ corresponding to a significance of 2.0σ. Note, this is *one* of the figures produced from the 10 repeated tests. (b) The unrelated field shows no significant clustering on any scale.

however, in figure 18(c), similar trajectory is also seen, but on other Mg II absorbers that were missed in figure 18(d). The two DESI cluster figures 18(c) and 18(d) have richness limits applied of $R \leq 22.5$ and $R \geq 22.5$, respectively, so the crossover of the two figures is minimal. (The median richness limit for the DESI clusters is 22.5 [49].) We might thus have a potentially useful technique of investigating the Mg II absorbers and their association with low and high richness clusters, from which we might learn more about the physical origin of the Mg II absorbers. We can also see in figure 19 the DESI clusters of all richnesses plotted in green contours over the BR Mg II absorbers. Comparison with figures 18(c) and 18(d), which are for $R \leq 22.5$ and $R \geq 22.5$, indicates that figure 19 shows the strongest association of the DESI clusters with the Mg II absorbers. Of course, the DESI clusters will have much larger redshift errors ($\Delta z \sim 0.04$) than the Mg II absorbers and quasars, so the structures in the DESI clusters will be blurred. Given that the association seems quite clear, then presumably smaller redshift errors would lead to an even clearer association.

4.2 Viewing the BR from other angles

The BR and GA discoveries were made unexpectedly with the method of intervening Mg II absorbers, and so are subject to observational bias — we have first detected the signal of a LSS by observing a curious shape and/or visual overdensity in the initial Mg II images that we later assess statistically. Specifically, we are only observing these LSS candidates from one line of sight (LOS), i.e., a 2D projection on the sky of the 3D matter distribution. Thus, from a different viewing angle, or LOS, the LSS candidates could look entirely different, or

JCAP07(2024)055

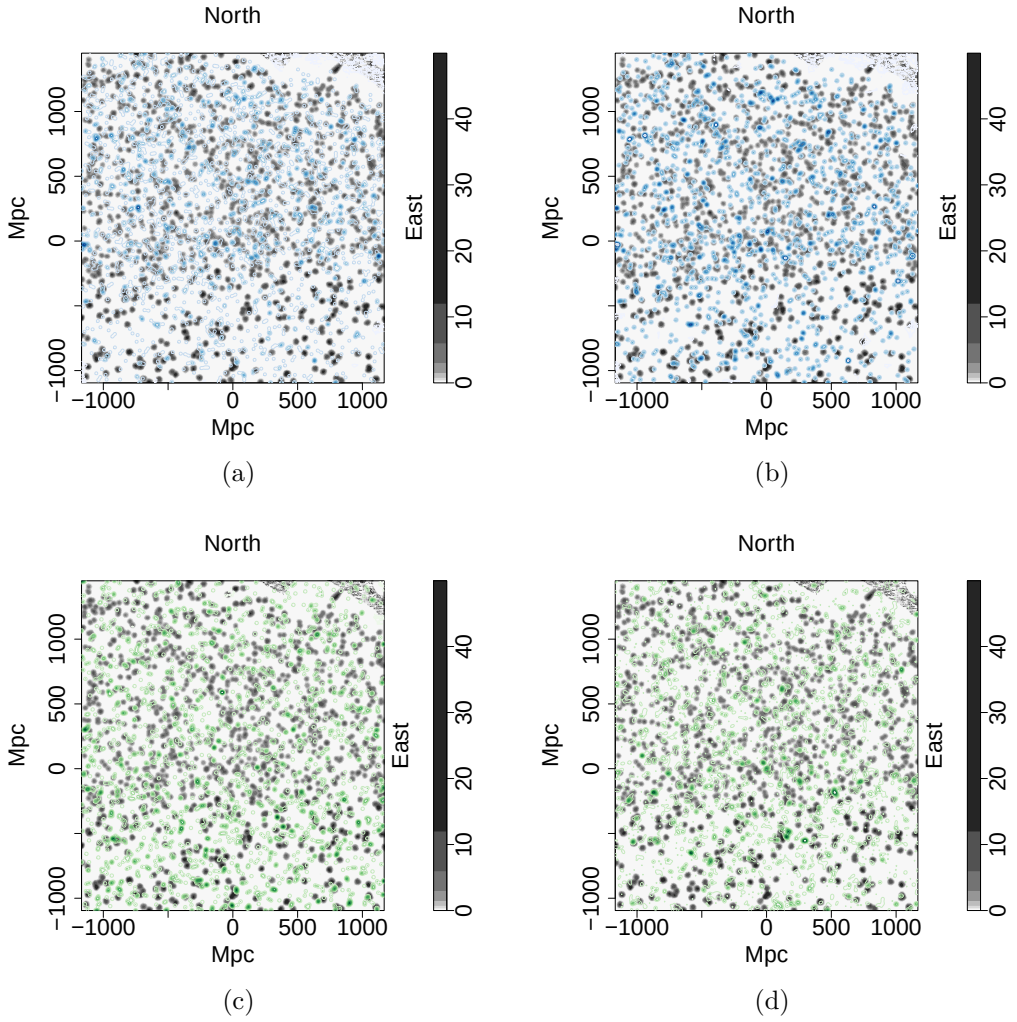

Figure 18. Density distribution of the Mg II absorbers in the redshift slice $z = 0.802 \pm 0.060$ in a large field-of-view represented by the grey contours which have been smoothed using a Gaussian kernel of $\sigma = 11$ Mpc and flat-fielded with respect to the background quasars. The additional contours (in blue and green) represent the superimposed density distribution of the field quasars (a and b) and the DESI clusters (c and d), respectively. (a) The field quasars, represented by the blue contours, are restricted to $i \leq 20.0$. The blue contours appear to have a plausible association with the grey contours. The i magnitude limit is not very restrictive so the blue contours are visually noisy compared with the Mg II absorbers. Note, these quasars were found to have a FilFinder filament that linked closely to the shape of the BR, so clearly it is the visual impression that is difficult to determine due to the noise. (b) The field quasars, represented by the blue contours, are restricted to $i \leq 19.5$. With the reduced quasars (compared with a) a clearer trend of quasar and Mg II absorber association can be seen. Generally, the dense clumps of Mg II absorbers appear to have associated quasars rather than the thin Mg II filaments. (c) The DESI clusters, represented by the green contours, are restricted to $R \leq 22.5$. The green contours generally follow the grey contours, although the richness limit reduces the number of DESI clusters in the field. (d) The DESI clusters, represented by the green contours, are restricted to $R \geq 22.5$. Again, it can be seen that the green contours generally follow the grey contours. In particular, the lower half of the BR has a strong filament of DESI clusters following the filamentary shape of the Mg II absorbers. Note, the larger field-of-view of the above figures crosses two of the SDSS borders where the quasar coverage drops sharply (see figure 5).

JCAP07(2024)055

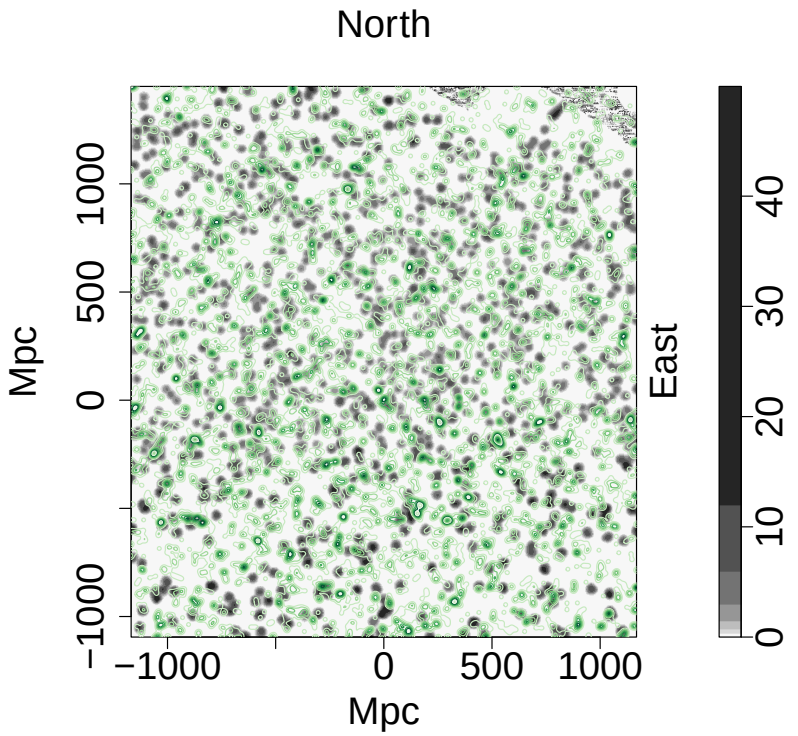

Figure 19. All of the DESI clusters with richnesses $0 < R \leq 300$, represented by the green contours. Here it can be seen that the green contours generally follow the grey contours quite well. Compare with figures 18(c) and 18(d), which are for $R \leq 22.5$ and $R \geq 22.5$. Note, the larger field-of-view of the figure crosses two of the SDSS borders where the quasar coverage drops sharply (see figure 5).

furthermore, there could be LSS candidates that have a seemingly average, or 'uninteresting' distribution of absorber members from our LOS that may be arcs, rings or interesting filamentary shapes from a different viewing angle.

We investigate how different viewing angles change the perception of the BR, which first requires redefining the coordinate system on which the BR-field absorber members are projected, described here. An initial, orthogonal, 3-vector coordinate system is defined such that u_0, v_0, w_0 are closely linked to $x_{\rm prop}, y_{\rm prop}, z_{\rm prop}$. The initial normal vector (w_0) is defined as the proper coordinate to the mean $x_{\rm prop}, y_{\rm prop}, z_{\rm prop}$ of the absorber members (which can be thought of as the original LOS). Then, the plane perpendicular to the normal is rotated such that u_0 points towards the most easterly absorber. Finally, all the absorber members are projected onto the new plane (see figure 20). Hence, we call this method the 'project-plane method'. With the initial coordinate system defined, we can define any new normal vector (w) as some combination of the initial u_0, v_0, w_0.

In figure 20 and other similar figures following, the colours of the absorbers indicate the redshift of each absorber, with the high-z absorbers represented by a darker shade, and vice versa (see the key on the top left of the figures). The numbers associated with each absorber are a simple ID system, labelled 1 to 51 in ascending order from the most easterly absorber to the most westerly (i.e., in descending order of RA). The ID system remains the same throughout all subsequent rotations of the plane projections so that the numbers can be used

JCAP07(2024)055

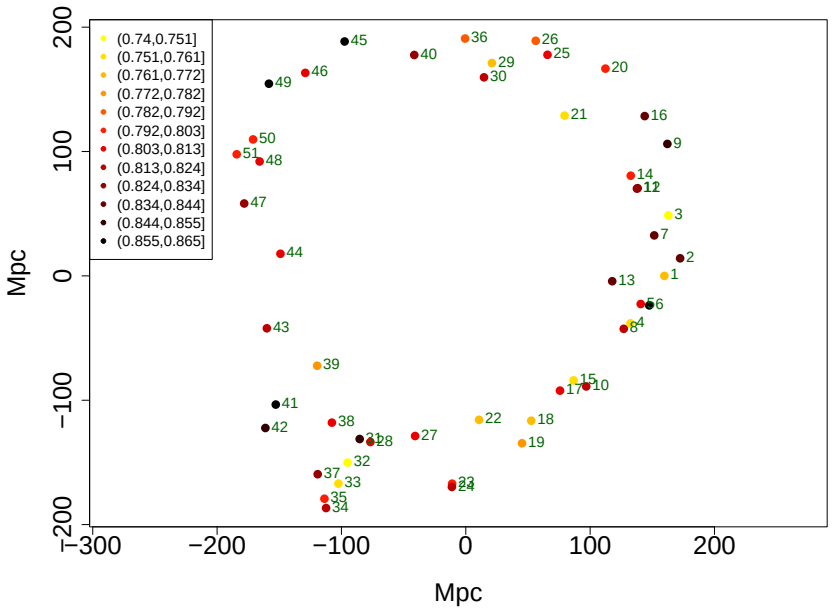

Figure 20. The visually-identified BR absorber members projected onto the plane perpendicular to the initial normal vector, w_0. The x-axis points towards the u_0 direction and the y-axis points towards the v_0 direction. By comparing the figure here with figure 2 one will notice the slight rotation of the BR projection, indicating the small misalignment of the tangent-plane coordinate system with the new u_0, v_0, w_0 system. The key in the top l.h.s. of the figure indicates the redshifts of the absorbers associated by the colours, and the small numbers paired with each data point indicate their unique ID number.

to orientate oneself. In this manner we are viewing the BR from different viewing angles, similar to taking snapshots of the 3D structure from different LOSs. Note, the observational analysis presented on the BR here is based on the visually selected BR absorber members, which are the blue points in figure 2.

We then redefine the normal with combinations of the original, orthogonal, 3-vector system to give different projected planes. The newly-defined vectors u, v, w are similarly orthogonal. Figures 21–23 have different viewing angles of the BR, and the observational analysis of each plane projection follows.

In figure 21 the new normal is set to u_0, which can be thought of as the side-on view of the BR. To emphasise this point, the redshift colours are banded vertically indicating that the u-axis has essentially become the redshift z-axis. Of interest in this figure is the curious backwards 'S' shape which is in both the dark-coloured high-z absorbers and the light-coloured low-z absorbers. The impression is that the BR has three distinct redshift bands, and the absorbers in each band create a noticeable backwards 'S' shape, but more so in the nearest and farthest redshift bins (the lightest and darkest coloured absorbers). It is not entirely clear what the backwards 'S' shape might indicate, or if it warrants further investigation. Initially, it could be thought that the absorbers belonging to the three distinct redshift bands may also be associated particularly with some of the SLHC identified groups from figure 7, but this is not the case. However, instead we find that almost all (one exception, starred in the list below) of the nearest redshift absorbers (those forming the backwards

JCAP07(2024)055

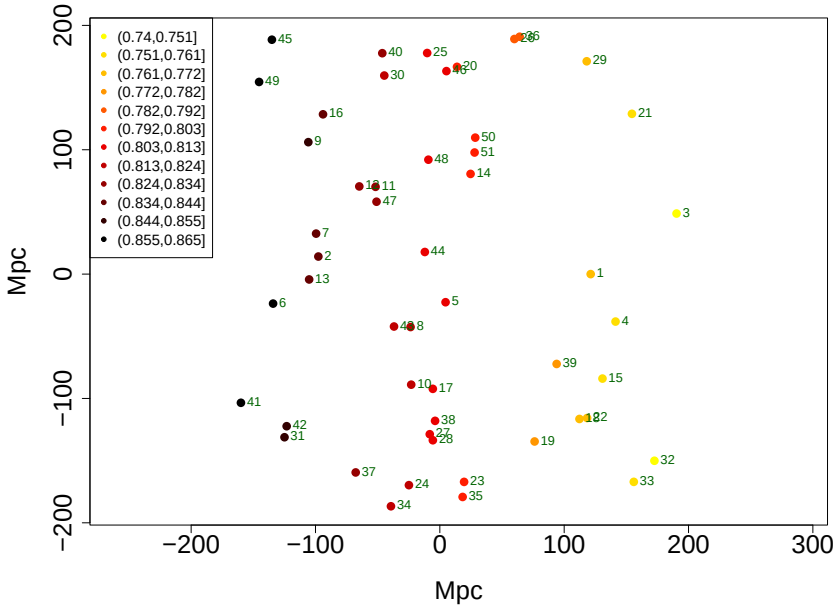

Figure 21. The BR absorber members projected onto the plane perpendicular to u_0. The new u direction points towards the most easterly absorber, as usual. The colours represent the redshifts of the absorbers (see the key in the top l.h.s. of the figure) and the small numbers paired with each data point indicate their unique ID number.

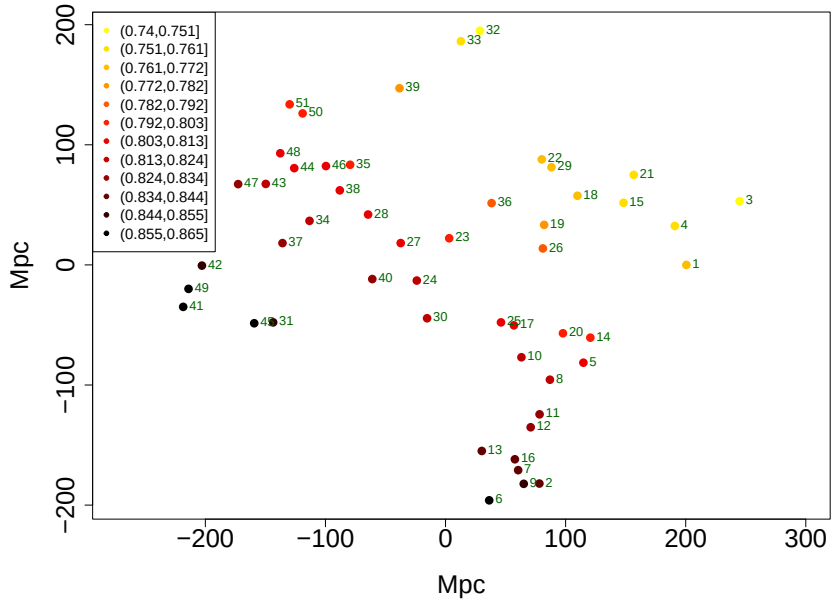

Figure 22. The BR absorber members projected onto the plane perpendicular to v_0. The new u direction points towards the most easterly absorber, as usual. The colours represent the redshifts of the absorbers (see the key in the top l.h.s. of the figure) and the small numbers paired with each data point indicate their unique ID number.

JCAP07(2024)055

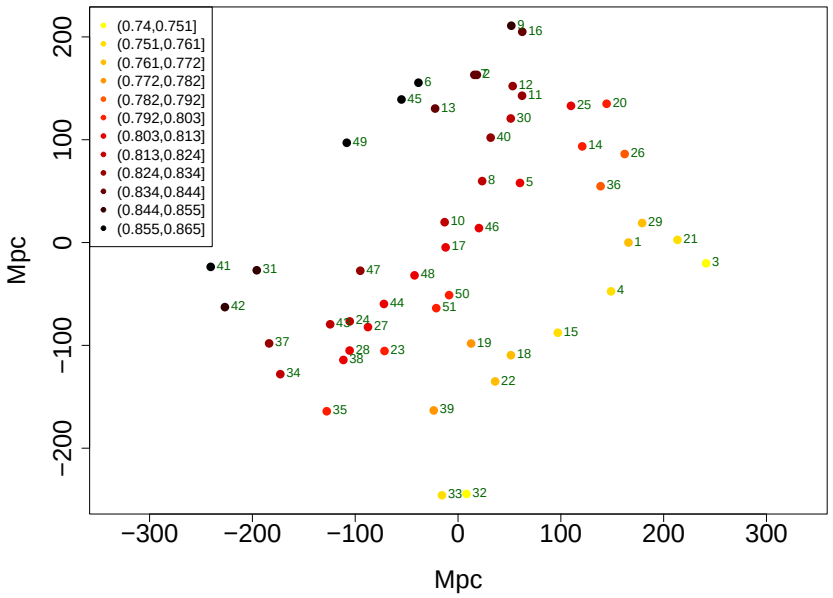

Figure 23. The BR absorber members projected onto the plane perpendicular to $u_0 - v_0$. The new u direction points towards the most easterly absorber, as usual. The colours represent the redshifts of the absorbers (see the key in the top l.h.s. of the figure) and the small numbers paired with each data point indicate their unique ID number.

'S' shape with the light-coloured absorbers) belong to one half of the BR closest to the r.h.s. This can be confirmed by cross-correlating the number IDs in figure 20 and figure 21. (IDs of absorbers contained in the near-redshift band, i.e., the light-coloured backwards 'S' shape: $36, 26, 29, 21, 3, 1, 4, 39*, 15, 22, 18, 19, 32, 33$. 39 has been starred as the one absorber belonging in the near-redshift band that does not sit with the rest of the absorbers on one half of the BR.) So the near-redshift absorbers form an arc of a circle closest to the r.h.s. of the BR. Later we will see that this further implies a somewhat spiral or 'cork-screw' interpretation of the BR, that is aligned face-on with our LOS.

In figure 22 the new normal is set to v_0, which can be thought of as viewing the BR from the bottom, looking up. Now we can see a thin, central arc which is formed from the most central redshift absorbers, with clumps of absorbers at lower and higher redshift either side of this arc. If the BR had been discovered from this particular angle, had we been located at a different position in the Universe, then we may have named this structure the 'Big Arc'. This highlights the observational bias mentioned earlier: our viewing angle only allows one LOS in which to discover interesting structures and filaments when using the Mg II image method. However, it also presents the opportunity to re-examine LSS candidates from multiple viewing angles.

In figure 23 the new normal is set to $u_0 - v_0$, which can be thought of as looking at 45° through the BR towards the south-east direction. The BR now very clearly resembles that of a coil, and the inner filament is very thin and filamentary. The high-z and low-z absorbers form ovoid shapes connected by the inner filament, although the high-z absorbers appear more broken and sparse compared with the rest of the coil.

All three viewing angles, plus the original face-on view of the BR, indicate that the BR structure is a coil shape with a thin, flat, dense, central component. The flatness of the

JCAP07(2024)055

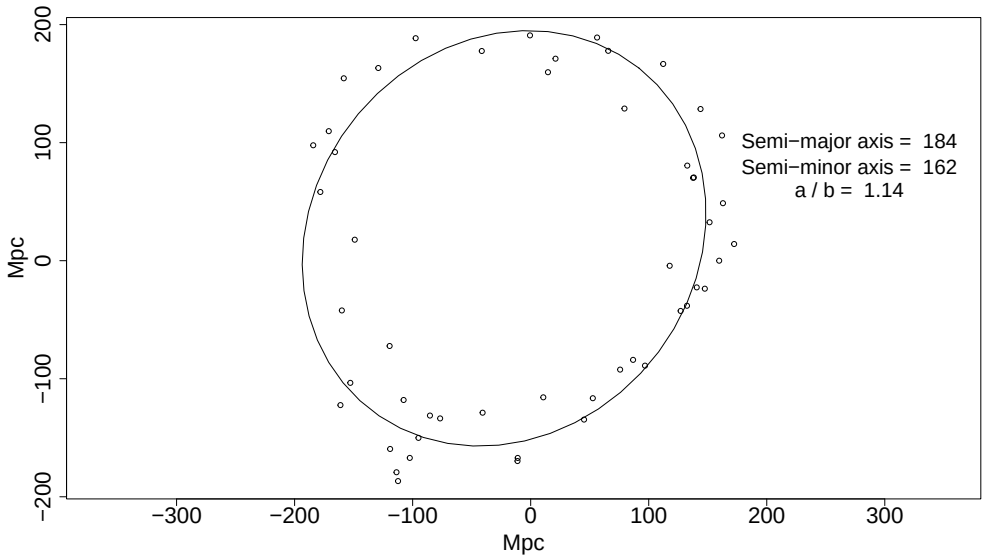

Figure 24. The visually-identified BR absorber members projected onto the plane perpendicular to w_0 with an added fitted ellipse.

central component is particularly interesting given the recent work of finding flat patterns in cosmic structure presented in [17]. It is not yet clear how a structure like this will have formed; however, one possibility could be cosmic strings, which have been suggested to explain other recent discoveries and data [16, 17, 41–46].

Previously, the diameter of the BR was noted as similar to the expected size of a BAO. However, the coil shape seems likely to be inconsistent with an origin in BAOs.

Finally, an ellipse can be fitted to the BR (figure 24). The ellipse calculates the semi-major and semi-minor axes as 184 Mpc and 162 Mpc, respectively. Given that the signature of an individual BAO has a characteristic size of 150 Mpc, we again argue against the possibility of the BR occurring from a BAO. Given the ellipse calculations of the semi-major and semi-minor axes we can use Ramanujan's approximative perimeter to approximate the circumference of the ellipse,

$$p_R = \pi\left\{(a+b) + \frac{3(a-b)^2}{10(a+b)+\sqrt{a^2+14ab+b^2}}\right\}$$

where a and b are the semi-major and semi-minor axes. The circumference of the ellipse is then $\sim$ 1.1 Gpc.

4.3 Equivalent widths

In figure 20 we showed the visually-identified BR absorber members projected onto a plane normal to the vector w_0 (which corresponds to the LOS), with the points colour-coded according to redshift. Here, in figure 25, we show a corresponding figure but with the points now colour-coded according to the rest-frame equivalent widths (in Å) of the λ_{2796} component of the Mg II doublet. The equivalent widths and their uncertainties, both taken from the Mg II database of [3], are tabulated in table 5.

JCAP07(2024)055

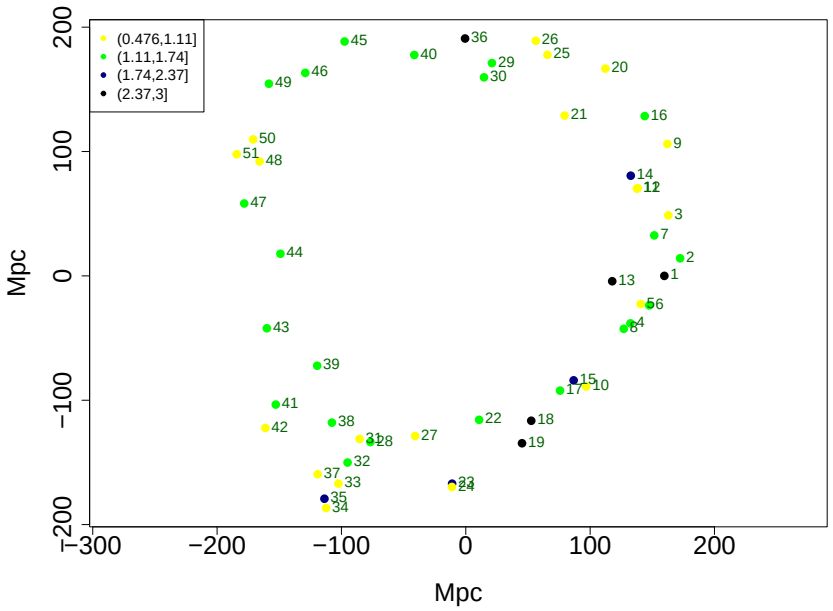

Figure 25. The visually-identified BR absorber members projected onto the plane perpendicular to the initial normal vector, w_0. The x-axis points towards the u_0 direction and the y-axis points towards the v_0 direction. The key in the top l.h.s. of the figure indicates the rest-frame equivalent widths (in Å) of the λ_{2796} component of the absorbers associated by the colours, and the small numbers paired with each data point indicate their unique ID number. The equivalent widths are taken from the Mg II database of [3].

In figure 25 there is no obvious pattern for the lower equivalent widths, but we note that the higher equivalent widths tend to be concentrated on the r.h.s. of the plot, especially the points that are numbered $14, 1, 13, 15, 18, 19, 23$ (but not $36, 35$).

The earlier figure 23, for the plane perpendicular to $u_0 - v_0$, drew attention to ovoid shapes at high-z and low-z. Here, figure 26 corresponds to that figure, but again with colour-coding according to the equivalent widths. It shows that the points $14, 36, 1, 15, 18, 19$ (and possibly $23, 35$ but not 13) are actually concentrated in the low-z ovoid shape. Possibly a preferential alignment with respect to the LOS of the host galaxies in this ovoid shape is enhancing the column densities.

5 Discussion and conclusions

In this paper we have presented a 'Big Ring on the Sky', which is the second ultra-large large-scale structure (uLSS) detected in the Mg II catalogues The BR is detected most prominently in the redshift slice $z = 0.802 \pm 0.060$. The redshift slice containing the BR is the exact same redshift slice containing the previously detected GA, and both structures on the sky are separated by only $\sim 12°$, meaning that these two intriguing structures are in the same cosmological neighbourhood.

We applied several inspection tests and statistical tests to the BR to support it as an ultra-large LSS. A summary of the results is as follows. (1) Each of the visually-identified BR+filament absorbers was confirmed visually in the corresponding spectra, establishing that

JCAP07(2024)055

ID	EW (Å)	$\sigma_{\rm EW}$ (Å)	ID	EW (Å)	$\sigma_{\rm EW}$ (Å)
1	2.99	0.17	**27**	0.96	0.12
2	1.46	0.20	**28**	1.15	0.27
3	0.94	0.12	**29**	1.63	0.19
4	1.71	0.43	**30**	1.35	0.30
5	1.05	0.23	**31**	0.76	0.09
6	1.29	0.26	**32**	1.22	0.30
7	1.13	0.28	**33**	0.93	0.12
8	1.31	0.22	**34**	0.99	0.18
9	0.51	0.13	**35**	2.07	0.43
10	0.72	0.15	**36**	2.49	0.35
11	1.08	0.06	**37**	0.51	0.05
12	0.82	0.05	**38**	1.33	0.16
13	2.70	0.46	**39**	1.32	0.29
14	2.29	0.32	**40**	1.20	0.22
15	1.75	0.25	**41**	1.73	0.33
16	1.45	0.32	**42**	0.76	0.05
17	1.55	0.36	**43**	1.28	0.25
18	2.62	0.08	**44**	1.50	0.17
19	2.58	0.21	**45**	1.35	0.12
20	1.07	0.05	**46**	1.55	0.25
21	0.86	0.05	**47**	1.50	0.36
22	1.66	0.12	**48**	0.91	0.21
23	2.08	0.20	**49**	1.56	0.29
24	1.05	0.25	**50**	0.48	0.11
25	0.79	0.09	**51**	1.08	0.11
26	0.58	0.09			

Table 5. The table is for the 51 visually-identified BR absorber members. The identification numbers (ID) correspond to those in figure 20 and the other similar figures that follow it. The rest-frame equivalent widths (EW) and their associated uncertainties ($\sigma_{\rm EW}$, taken from the Mg II database of [3], are for the λ_{2796} component of the Mg II doublet; the units are Å. Note that the EW for point 12 is likely to be enhanced by the superimposed λ_{2803} component from point 11.

100% of the absorbers are real detections, and not false-positives. (2) The SLHC algorithm identified 46 out of 59 of the visually-identified BR+filament absorbers across 5 individual, overlapping or adjacent, groups. The SLHC algorithm also detected a statistically-significant arc in the redshift slices centred at $z = 0.862 \pm 0.060$ and $z = 0.922 \pm 0.060$. The arc appears to be an extension of the bottom arc of the BR, given the agreement in the on-sky position and that the redshift slices overlap by 50%. (3) We calculated the CHMS and MST significance of the SLHC-identified absorbers, the visually-identified BR absorbers (two versions), and the FilFinder-identified absorbers. The CHMS method was found to have a much larger variation in its reported significances due to the nature of the method: the CHMS calculates the volume

JCAP07(2024)055

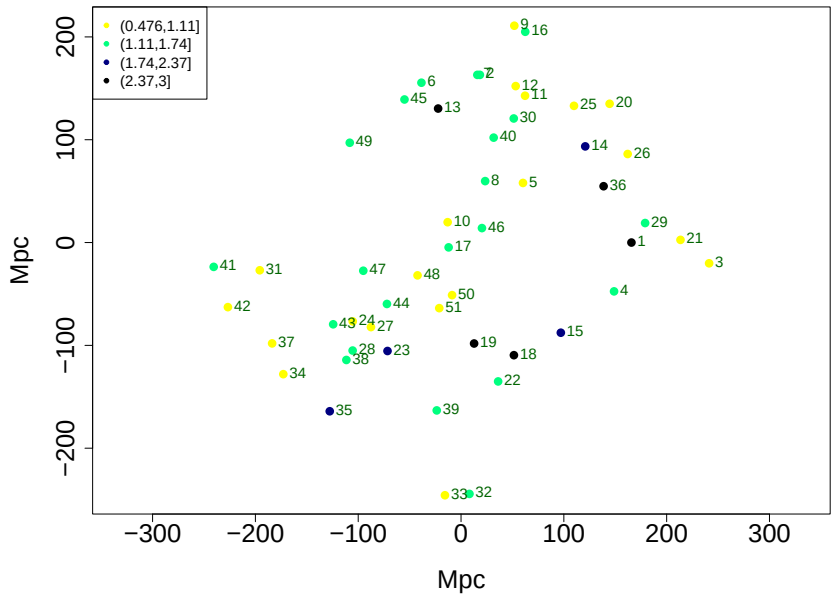

Figure 26. The BR absorber members projected onto the plane perpendicular to $u_0 - v_0$. The new u direction points towards the most easterly absorber, as usual. The key in the top l.h.s. of the figure indicates the rest-frame equivalent widths (in Å) of the λ_{2796} component of the absorbers associated by the colours, and the small numbers paired with each data point indicate their unique ID number. The equivalent widths are taken from the Mg II database of [3].

of the unique structure containing all the absorbers, so in the example of a ring-like structure, there is a large volume in the centre of the ring with far fewer absorbers than the annulus. The CHMS calculates a $(3.65 \pm 1.13)\sigma$ significance. By using the visually-identified absorbers, and keeping the BR innards, the CHMS calculates a (likely) upper limit of 5.2σ significance. The MST significance on the other hand was more consistent, as this method relies only on the mean MST edge-length, and this method calculates a significance of $(4.10 \pm 0.45)\sigma$. (4) The FilFinder algorithm was applied to the Mg II image of the BR field to identify filaments objectively. By incrementally increasing the size-threshold, the algorithm left only one identified filament — a ring — and that ring corresponded to the visually-identified BR. In this way, the BR was established as: (i) a ring, independently of visual perception; and (ii) the most-connected and largest filament in the image. We also applied the FilFinder algorithm to the field quasars (not to be confused with the background probes) and this found that there was a large, connected, ring-like filament that mostly aligns with the BR. (5) We applied the CE test to the field containing the BR and then 'zoomed' in on the BR to assess the contribution of the BR to the spatial clustering in the field. Tentative significant clustering in the field was detected in the second zoom of the BR, at a p-value $p = 0.022$ (corresponding to a significance of 2.0σ). We compared this with four other unrelated fields at the same redshift as the BR and found no significant spatial clustering. However, the CE test results for the BR field are still inconclusive at the $\sigma > 3.0$ significance level, suggesting that the clustering in the BR field is not statistically significant, unlike what was seen with the GA field. Note, this test assesses the clustering in the *field* and not the statistical significance of any individual candidate structure. (6) By superimposing contour maps of the field quasars

JCAP07(2024)055

and DESI clusters on the Mg II absorber images we were able to show plausible association between the datasets, thus providing independent corroboration. We found in particular that the DESI clusters that were subject to richness limits were mapping different Mg II absorbers, suggesting that there could be scope for using DESI clusters as a way to investigate the physical environment around the Mg II absorbers. (7) Using a project-plane method we could investigate the 3D distribution of the BR. Viewing the BR on different angles showed that there are 3 distinct redshift bands, where the central redshift band contains the majority of the absorbers in a ring shape in a thin, flat region. The near-redshift band is contained almost entirely on the r.h.s. of the BR and even appears to angle backwards into the central redshift bin of the BR creating a spiral-like shape. The farthest-redshift band had a similar coiling effect, but appeared to be distributed randomly throughout the BR (it made a broken, ring shape). We also found, with the project-plane method, curious backwards 'S' shapes when viewing the BR side on. The S shapes are most apparent in the near and far redshift bands but can also be seen in the central redshift band.

The data and analysis show that the BR is of particular interest for LSS studies in cosmology. In cosmology, we assume statistical homogeneity in the Cosmological Principle (CP) as the foundations of the ΛCDM model. We have shown that the BR is real and statistically significant, adding it to a growing list of LSS candidates that are in tension with the CP. The growing list of LSSs also indicates that the chance of all of these structures being a matter of statistical noise is decreasing. In addition, the list of LSSs in tension with the CP is also generally difficult to understand as there are gaps in the knowledge for explaining the formation of these ultra-large structures. Perhaps we could speculate that the existence of these structures requires an extension to the standard model, perhaps in the form of cosmic strings.

The BR and GA together, given their sizes and morphologies, are presumably telling us something intriguing, and quite possibly important, about the Universe, but at the moment we can only speculate what that might be.

Acknowledgments

We acknowledge the use of the public R software (v4.1.2).[4] Our data has depended on the publicly-available Sloan Digital Sky Survey quasar catalogue and the corresponding Mg II catalogues.[5] AML was supported by a UCLan/JHI PhD studentship.

We thank the referee for thoughtful comments and useful suggestions.

[4] https://www.R-project.org/.

[5] https://wwwmpa.mpa-garching.mpg.de/SDSS/MgII/.

JCAP07(2024)055

References

[1] A.M. Lopez, *Assessing the potential of intervening Mg* II *absorbers for cosmology*, M.Sc. Thesis, University of Central Lancashire (2019).

[2] A.M. Lopez, R.G. Clowes and G.M. Williger, *A Giant Arc on the Sky*, *Mon. Not. Roy. Astron. Soc.* **516** (2022) 1557 [arXiv:2201.06875] [INSPIRE].

[3] A. Anand, D. Nelson and G. Kauffmann, *Characterizing the abundance, properties, and kinematics of the cool circumgalactic medium of galaxies in absorption with SDSS DR16*, *Mon. Not. Roy. Astron. Soc.* **504** (2021) 65 [arXiv:2103.15842] [INSPIRE].

[4] G. Zhu and B. Ménard, *The JHU-SDSS metal absorption line catalog: redshift evolution and properties of Mg II absorbers*, *Astrophys. J.* **770** (2013) 130 [arXiv:1211.6215] [INSPIRE].

[5] J. Bergeron, *Galaxies Giving Rise to MgII Absorption Systems in Quasar Spectra*, in the proceedings of the *130th Symposium of the IAU on Large scale structures of the Universe*, Balatonfured, Hungary, 15–20 June 1987, DOI:10.1017/s007418090013623x.

[6] C.W. Churchill, G.G. Kacprzak and C.C. Steidel, *MgII absorption through intermediate redshift galaxies*, in the proceedings of the *IAU Colloquium 199: Probing Galaxies throught Quasar Absporption Lines*, Shanghai, People's Republic of China, 14–18 March 2005 [DOI:10.1017/S1743921305002401] [astro-ph/0504392] [INSPIRE].

[7] C.C. Steidel, *The nature and evolution of absorption: Selected galaxies*, in the proceedings of the *ESO Workshop on QSO absorption lines*, Garching, Germany, November 1994 [astro-ph/9509098] [INSPIRE].

[8] J. Bagchi et al., *Saraswati: An Extremely Massive* ~ 200 *Megaparsec Scale Supercluster*, *Astrophys. J.* **844** (2017) 25 [arXiv:1707.03082] [INSPIRE].

[9] L.G. Balázs et al., *A giant ring-like structure at* $0.78 < z < 0.86$ *displayed by GRBs*, *Mon. Not. Roy. Astron. Soc.* **452** (2015) 2236 [arXiv:1507.00675] [INSPIRE].

[10] I. Horváth, J. Hakkila and Z. Bagoly, *Possible structure in the GRB sky distribution at redshift two*, *Astron. Astrophys.* **561** (2014) L12 [arXiv:1401.0533] [INSPIRE].

[11] R.G. Clowes et al., *A structure in the early universe at* $z \sim 1.3$ *that exceeds the homogeneity scale of the R-W concordance cosmology*, *Mon. Not. Roy. Astron. Soc.* **429** (2013) 2910 [arXiv:1211.6256] [INSPIRE].

[12] R.G. Clowes, L.E. Campusano, M.J. Graham and I.K. Soechting, *Two close Large Quasar Groups of size* ~ 350 *Mpc at* $z \sim 1.2$, *Mon. Not. Roy. Astron. Soc.* **419** (2012) 556 [arXiv:1108.6221] [INSPIRE].

[13] P.K. Aluri et al., *Is the observable Universe consistent with the cosmological principle?*, *Class. Quant. Grav.* **40** (2023) 094001 [arXiv:2207.05765] [INSPIRE].

[14] D. Huterer, *Growth of cosmic structure*, *Astron. Astrophys. Rev.* **31** (2023) 2 [arXiv:2212.05003] [INSPIRE].

[15] P. Bari et al., *Signatures of Primordial Gravitational Waves on the Large-Scale Structure of the Universe*, *Phys. Rev. Lett.* **129** (2022) 091301 [arXiv:2111.06884] [INSPIRE].

[16] W. Ahmed, T.A. Chowdhury, S. Nasri and S. Saad, *Gravitational waves from metastable cosmic strings in the Pati-Salam model in light of new pulsar timing array data*, *Phys. Rev. D* **109** (2024) 015008 [arXiv:2308.13248] [INSPIRE].

[17] P.J.E. Peebles, *Flat patterns in cosmic structure*, *Mon. Not. Roy. Astron. Soc.* **526** (2023) 4490 [arXiv:2308.04245] [INSPIRE].

JCAP07(2024)055

[18] B. Shlaer, A. Vilenkin and A. Loeb, *Early structure formation from cosmic string loops*, *JCAP* **05** (2012) 026 [arXiv:1202.1346] [INSPIRE].

[19] R. Penrose, *On the Gravitization of Quantum Mechanics 2: Conformal Cyclic Cosmology*, *Found. Phys.* **44** (2014) 873 [INSPIRE].

[20] S. Mazurenko, I. Banik, P. Kroupa and M. Haslbauer, *A simultaneous solution to the Hubble tension and observed bulk flow within 250 h−1 Mpc*, *Mon. Not. Roy. Astron. Soc.* **527** (2024) 4388 [arXiv:2311.17988] [INSPIRE].

[21] C. Llinares, A. Knebe and H.S. Zhao, *Cosmological Structure Formation under MOND: a new numerical solver for Poisson's equation*, *Mon. Not. Roy. Astron. Soc.* **391** (2008) 1778 [arXiv:0809.2899] [INSPIRE].

[22] M. Milgrom, *A modification of the Newtonian dynamics as a possible alternative to the hidden mass hypothesis*, *Astrophys. J.* **270** (1983) 365 [INSPIRE].

[23] EBOSS collaboration, *The Sloan Digital Sky Survey Quasar Catalog: Sixteenth Data Release*, *Astrophys. J. Suppl.* **250** (2020) 8 [arXiv:2007.09001] [INSPIRE].

[24] SDSS collaboration, *The Sloan Digital Sky Survey Quasar Catalog V. Seventh Data Release*, *Astron. J.* **139** (2010) 2360 [arXiv:1004.1167] [INSPIRE].

[25] I. Pâris et al., *The Sloan Digital Sky Survey Quasar Catalog: twelfth data release*, *Astron. Astrophys.* **597** (2017) A79 [arXiv:1608.06483] [INSPIRE].

[26] R.B. Tully, C. Howlett and D. Pomarède, *Ho'oleilana: An Individual Baryon Acoustic Oscillation?*, *Astrophys. J.* **954** (2023) 169 [arXiv:2309.00677] [INSPIRE].

[27] M. Einasto et al., *Shell-like structures in our cosmic neighbourhood*, *Astron. Astrophys.* **587** (2016) A116 [arXiv:1506.05295] [INSPIRE].

[28] PLANCK collaboration, *Planck 2015 results. XIII. Cosmological parameters*, *Astron. Astrophys.* **594** (2016) A13 [arXiv:1502.01589] [INSPIRE].

[29] BOSS collaboration, *The clustering of galaxies in the SDSS-III Baryon Oscillation Spectroscopic Survey: baryon acoustic oscillations in the Data Releases 10 and 11 Galaxy samples*, *Mon. Not. Roy. Astron. Soc.* **441** (2014) 24 [arXiv:1312.4877] [INSPIRE].

[30] SDSS collaboration, *Detection of the Baryon Acoustic Peak in the Large-Scale Correlation Function of SDSS Luminous Red Galaxies*, *Astrophys. J.* **633** (2005) 560 [astro-ph/0501171] [INSPIRE].

[31] L. Napolitano et al., *Detecting and Characterizing Mg ii Absorption in DESI Survey Validation Quasar Spectra*, *Astron. J.* **166** (2023) 99 [arXiv:2305.20016] [INSPIRE].

[32] J.K. Yadav, J.S. Bagla and N. Khandai, *Fractal Dimension as a measure of the scale of Homogeneity*, *Mon. Not. Roy. Astron. Soc.* **405** (2010) 2009 [arXiv:1001.0617] [INSPIRE].

[33] M.B. Taylor, *TOPCAT & STIL: Starlink Table/VOTable Processing Software* in the proceedings of the *Astronomical Society of the Pacific Conference Series on Astronomical Data Analysis Software and Systems XIV*, Pasadena, California, U.S.A., 24–27 October 2004.

[34] D. Pomarède et al., *Cosmicflows-3: The South Pole Wall*, *Astrophys. J.* **897** (2020) 133 [arXiv:2007.04414] [INSPIRE].

[35] I.I.J.R. Gott et al., *A map of the universe*, *Astrophys. J.* **624** (2005) 463 [astro-ph/0310571] [INSPIRE].

[36] S.V. Pilipenko, *The space distribution of quasars*, *Astron. Rep.* **51** (2007) 820.

JCAP07(2024)055

[37] E.W. Koch and E.W. Rosolowsky, *Filament Identification through Mathematical Morphology*, arXiv:1507.02289.

[38] B. Mookerjea et al., *Spiral Structure and Massive Star formation in the Hub-Filament-System G326.27-0.49*, *Mon. Not. Roy. Astron. Soc.* **520** (2023) 2517 [arXiv:2301.09775].

[39] S. Zhang et al., *ATOMS: ALMA Three-millimeter Observations of Massive Star-forming regions — XIII. Ongoing triggered star formation within clump-fed scenario found in the massive* ($\sim 1500\,M_\odot$) *clump*, *Mon. Not. Roy. Astron. Soc.* **520** (2023) 322 [arXiv:2301.01937].

[40] S.E. Meidt et al., *PHANGS-JWST First Results: ISM structure on the turbulent Jeans scale in four disk galaxies observed by JWST and ALMA*, *Astrophys. J. Lett.* **944** (2023) L18 [arXiv:2212.06434].

[41] B. Cyr, J. Chluba and S.K. Acharya, *Cosmic string solution to the radio synchrotron background*, *Phys. Rev. D* **109** (2024) L121301 [arXiv:2308.03512] [INSPIRE].

[42] J. Ellis, M. Lewicki, C. Lin and V. Vaskonen, *Cosmic superstrings revisited in light of NANOGrav 15-year data*, *Phys. Rev. D* **108** (2023) 103511 [arXiv:2306.17147] [INSPIRE].

[43] Y. Gouttenoire and E. Vitagliano, *Domain wall interpretation of the PTA signal confronting black hole overproduction*, arXiv:2306.17841 [INSPIRE].

[44] H. Jiao, R. Brandenberger and A. Refregier, *Early structure formation from cosmic string loops in light of early JWST observations*, *Phys. Rev. D* **108** (2023) 043510 [arXiv:2304.06429] [INSPIRE].

[45] S. Sanyal, *Nambu Goto cosmic strings in the early universe*, *Eur. Phys. J. ST* **231** (2022) 83 [INSPIRE].

[46] Z. Wang et al., *The nanohertz stochastic gravitational wave background from cosmic string loops and the abundant high redshift massive galaxies*, *Sci. China Phys. Mech. Astron.* **66** (2023) 120403 [arXiv:2306.17150] [INSPIRE].

[47] J. Cuzick and R. Edwards, *Spatial Clustering for Inhomogeneous Populations*, *J. Roy. Statist. Soc. B* **52** (1990) 73.

[48] J. French, *Statistical methods for the analysis of case-control point data*, CRAN, https://cran.r-project.org/web/packages/smacpod/ (2023).

[49] J. Gao et al., *Galaxy Clusters from the DESI Legacy Imaging Surveys. I. Cluster Detection*, *Astrophys. J. Suppl.* **253** (2021) 56 [arXiv:2101.12340] [INSPIRE].

JCAP07(2024)055